

Single-particle edge state in a local-resonance-induced topological band gap

Garigipati Sai Srikanth,^{1,*} Kai Qian,^{2,3,*} Ian Frankel,^{2,*} Georgios Theocharis,⁴ Nicholas Boechler,^{2,5} and Rajesh Chaunsali^{1,†}

¹*Department of Aerospace Engineering, Indian Institute of Science, Bangalore 560012, India*

²*Department of Mechanical and Aerospace Engineering, University of California, San Diego, La Jolla, CA 92093, USA*

³*George W. Woodruff School of Mechanical Engineering, Georgia Institute of Technology, Atlanta, GA 30332, USA*

⁴*Laboratoire d'Acoustique de l'Université du Mans (LAUM), UMR 6613, Institut d'Acoustique – Graduate School (IA-GS), CNRS, Le Mans, France*

⁵*Program in Materials Science and Engineering, University of California, San Diego, La Jolla, CA 92093, USA*

(Dated: March 9, 2026)

Topological metamaterials promise unprecedented wave control. Here, we theoretically and numerically investigate a one-dimensional Su-Schrieffer-Heeger (SSH) inspired stiffness dimer modified with a local resonator, which imparts a frequency-dependent effective stiffness to the unit cell. We demonstrate a two-step mechanism to create a topological local-resonance-induced band gap (LRG): first, a conventional Bragg-type band gap (BrG) is made topologically non-trivial via band inversion at a Dirac point; second, by tuning a dimerization parameter, the character of this non-trivial BrG is switched to that of an LRG via an intermediate flat band state. This process preserves the non-trivial topology without requiring gap closure within the LRG. Crucially, we find that when the resulting topological edge state intersects a characteristic frequency of the LRG—specifically, an attenuation singularity where the effective stiffness vanishes—it achieves extreme localization of vibrational energy. This state is confined to a single particle at the boundary, resulting in an inverse participation ratio of exactly unity, the theoretical limit for localization in a discrete system. Further, we demonstrate that while random disorder scatters the frequency of this mode, introducing tuned boundaries stabilizes the single-particle mode over a broad parameter range. Our findings provide a clear pathway to designing ultra-localized, topologically protected states in low-frequency regimes.

I. INTRODUCTION

Engineered materials, such as phononic crystals and acoustic metamaterials, provide powerful platforms for controlling wave propagation. One of their defining features is the ability to create frequency band gaps—spectral ranges where wave propagation is attenuated. These band gaps typically arise through two distinct physical mechanisms. The first is Bragg scattering, where coherent scattering from a periodic lattice opens so-called Bragg-type band gaps (BrGs) [1]. The second is local resonance, achieved by embedding resonant substructures into a host medium. These local resonators give rise to effective material properties (*e.g.*, dynamic mass density or modulus) that can vanish or diverge at characteristic frequencies, creating local-resonance-induced band gaps (LRGs) [2–7]. While both types of band gaps inhibit wave propagation, in addition to their differing physical origins, they differ in their attenuation profiles. In particular, given similar constituent materials and spatial periodicity, LRGs generally exhibit much sharper attenuation than BrGs [8, 9], with the attenuation often confined almost entirely to the first unit cell [10], and are capable of attenuating lower-frequency, larger-wavelength waves [11, 12].

Parallel to these developments, the introduction of topological band theory into mechanical systems has catalyzed the vibrant field of topological mechanics [13, 14]. In these systems, robust boundary modes (or states) emerge at edges [15], interfaces [16], and corners [17]. Residing deep within band gaps, these states exhibit remarkable resilience to disorder and imperfections due to their underlying topological protection. This intrinsic robustness makes them prime candidates for next-generation applications in fault-tolerant, one-way passive waveguiding, logic, and signal processing. When combined with the high attenuation characteristic of LRGs, we envision topological states with qualitatively superior localization properties compared to those hosted in BrGs: specifically, edge modes localized to a single particle at the boundary, representing the theoretical limit of confinement in a discrete system.

Localized boundary modes have been previously reported in resonant band gaps. For example, Zhang *et al.* [18] introduced resonator pairs into a classical valley-Hall lattice to obtain edge modes in resonant ranges, and Xia *et*

* These authors contributed equally.

† rchaunsali@iisc.ac.in

al. [19] demonstrated edge modes in a beam with quasi-periodically attached resonators. In these studies, however, the mechanism governing the topological transition from a trivial to a non-trivial LRG was largely unexplored. This question is non-trivial: conventional topological states at finite frequencies arise through band inversion at Dirac points, requiring gap closure and reopening [Fig. 1(a)]. Yet, in LRGs, the attenuation singularity—associated with vanishing effective stiffness (equivalently, diverging effective mass)—enforces a non-vanishing minimum gap width [20], thereby preventing gap closure under continuous parameter tuning [21]. A recent study by Jang *et al.* [22] resolved this through a two-step process: first inducing a topological transition within a BrG, and subsequently switching its gap character to an LRG, thus bypassing the need for gap closure within the LRG itself [Fig. 1(b)]. Similarly, Zhang *et al.* [23] illustrated a BrG-to-LRG transition in a beam-resonator system.

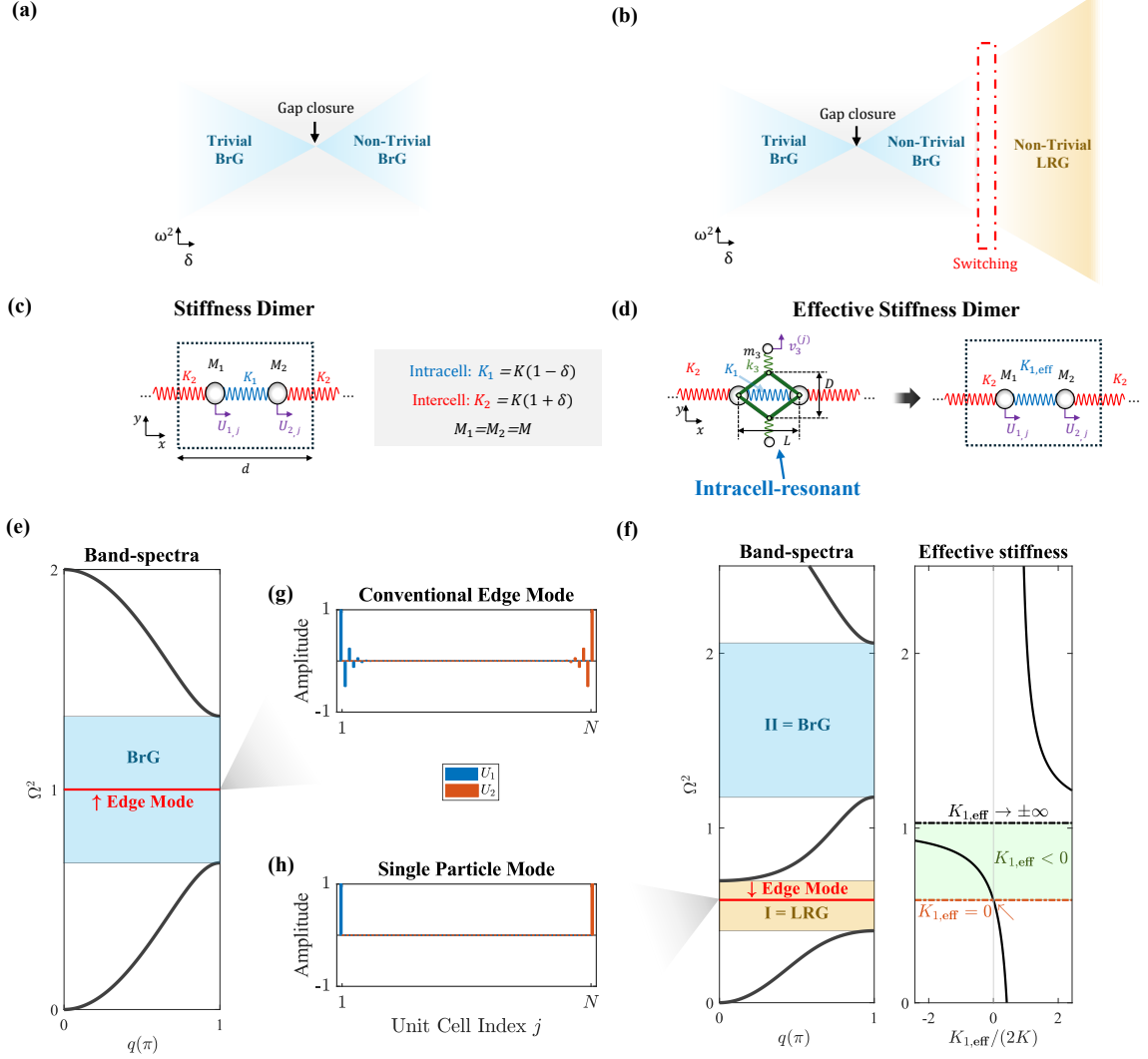


FIG. 1. Comparison of topological edge modes in a Bragg-type band gap (BrG) and an effective stiffness local-resonance-induced band gap (LRG). (a) Band closure and reopening driving topological transition in a BrG. (b) Pathway to topologically non-trivial LRG via gap-type switching from a non-trivial BrG. (c) Unit cell of conventional stiffness dimer chain. (d) Unit cell of effective stiffness dimer chain with local resonators (m_3, k_3). (e) Band structure of conventional dimer; blue region denotes BrG, red line indicates edge mode. (f) Left: Band structure of effective stiffness dimer with BrG (blue, II) and LRG (yellow, I). Right: $K_{1,\text{eff}}$ versus a normalized $\Omega^2 = \omega^2 M / (K_1 + K_2)$; orange dashed line marks $K_{1,\text{eff}} = 0$. (g) Edge mode profile in conventional dimer showing exponential decay. (h) Single-particle mode (SPM), localized on the edge with IPR=1, in the effective stiffness dimer. Parameters: $K_1 = 1$, $K_2 = 1.4286$, $M = 1$, $k_3 = 0.5$, $m_3 = 0.2$, $\lambda = 1$, $N = 60$ unit cells with fixed boundaries.

In this study, we present a three-band effective stiffness model that demonstrates a topological transition within a BrG, followed by a switch to an LRG, thereby rendering the LRG topologically nontrivial. Specifically, we consider

a modified version of the conventional SSH-inspired stiffness dimer chain [composed of equal masses connected by alternating springs, as shown in Fig. 1(c)], where a truss-based local resonator is attached to the intracell spring [as shown in Fig. 1(d), which we refer to as the *effective stiffness dimer chain*]. We show that, as we sweep a stiffness-dimerization parameter, the switch from the topologically nontrivial BrG to LRG involves the LRG-based attenuation singularity (zero effective stiffness) crossing from one gap to another, exactly at the flat-band formation, while preserving band topology. Furthermore, when a topological edge state intersects this singularity, it becomes confined to a single particle at the boundary, creating a *single-particle mode* (SPM). This level of confinement of the SPM represents the theoretical maximum for localization in a discrete system and, to the best of our knowledge, has not been demonstrated in previous studies (*e.g.*, Ref. [22] demonstrates near, but not the maximum confinement of the edge mode). Finally, we demonstrate that the SPM can be spectrally pinned by boundary tuning, enabling a finite parameter range where it remains robust under random disorder.

The remainder of this paper is organized as follows. Section II presents the results: Sec. II A introduces the unit-cell dynamics and effective model; Sec. II B details band gap characterization and the switching mechanism; Sec. II C analyzes the topological transition via band inversion; Sec. II D examines the finite chain spectrum and edge state localization; and Sec. II E discusses disorder analysis and tuned boundaries. Section III concludes with a summary and outlook.

II. RESULTS

A. Unit-cell dynamics and effective model

We begin by introducing the model, its equations of motion, and the corresponding dynamical matrix. Our system is a quasi-one-dimensional diatomic lattice, as illustrated in Fig. 1(d). Each unit cell consists of two identical primary masses M , constrained to horizontal motion, with displacements denoted by U_1 and U_2 . The primary masses are coupled by alternating linear springs of stiffness K_1 (intracell) and K_2 (intercell). The intracell spring is modified by a symmetric truss-type local-resonator structure proposed in Ref. [24]. This structure comprises a pair of identical local resonators, each consisting of a mass m_3 and a spring k_3 , coupled to the main chain through a hinged, massless truss mechanism. The resonator masses are constrained to vertical motion with displacement denoted by v_3 . As a result, the intracell coupling becomes frequency dependent.

The linearized equations of motion governing the j th unit cell are given by:

$$M\ddot{U}_{1,j} + K_1(U_{1,j} - U_{2,j}) + K_2(U_{1,j} - U_{2,j-1}) - k_3\lambda \left[v_{3,j} + \frac{\lambda}{2}(U_{2,j} - U_{1,j}) \right] = 0, \quad (1)$$

$$M\ddot{U}_{2,j} + K_1(U_{2,j} - U_{1,j}) + K_2(U_{2,j} - U_{1,j+1}) + k_3\lambda \left[v_{3,j} + \frac{\lambda}{2}(U_{2,j} - U_{1,j}) \right] = 0, \quad (2)$$

$$m_3\ddot{v}_{3,j} + k_3 \left[v_{3,j} + \frac{\lambda}{2}(U_{2,j} - U_{1,j}) \right] = 0, \quad (3)$$

where $\lambda = L/D$ characterizes the geometry of the truss mechanism, relating the horizontal displacement of the primary masses to the vertical displacement of the resonator (see Sec. I A of the Supplemental Material for geometric details). The terms involving $k_3\lambda$ represent the coupling forces transmitted through the truss mechanism.

Applying Bloch's theorem with the ansatz $U_{n,j} = U_n e^{i(qj - \omega t)}$ and $v_{3,j} = v_3 e^{i(qj - \omega t)}$ transforms these equations into a 3×3 eigenvalue problem, $\mathbf{D}(q)\mathbf{U} = \omega^2\mathbf{U}$, where $\mathbf{U} = [U_1, U_2, \sqrt{2m_3/M}v_3]^T$ is the eigenvector of modal amplitudes. The full dynamical matrix $\mathbf{D}(q)$ is:

$$\mathbf{D}(q) = \begin{pmatrix} \frac{K_1 + K_2}{M} + \frac{k_3\lambda^2}{2M} & -\left(\frac{K_1}{M} + \frac{K_2}{M}e^{-iq} + \frac{k_3\lambda^2}{2M}\right) & -\frac{k_3\lambda}{\sqrt{2Mm_3}} \\ -\left(\frac{K_1}{M} + \frac{K_2}{M}e^{iq} + \frac{k_3\lambda^2}{2M}\right) & \frac{K_1 + K_2}{M} + \frac{k_3\lambda^2}{2M} & \frac{k_3\lambda}{\sqrt{2Mm_3}} \\ -\frac{k_3\lambda}{\sqrt{2Mm_3}} & \frac{k_3\lambda}{\sqrt{2Mm_3}} & \frac{k_3}{m_3} \end{pmatrix}, \quad (4)$$

with $q = \tilde{\nu}d$ being the normalized wavenumber, where d being the lattice constant and $\tilde{\nu}$ being the wavenumber. The diagonal elements represent on-site stiffness contributions, while the off-diagonal elements encode coupling between Degrees of Freedom (DoF).

To facilitate comparison with a standard stiffness dimer and gain deeper physical insight, we employ an effective medium framework. The local resonator dynamics [Eq. (3)] can be solved algebraically for harmonic motion at frequency ω :

$$v_3 = -\frac{\lambda}{2} \frac{\omega_r^2}{\omega_r^2 - \omega^2} (U_2 - U_1), \quad (5)$$

where $\omega_r = \sqrt{k_3/m_3}$ is the natural frequency of the local resonators. Substituting this back into Eqs. (1) and (2), the entire intracell mechanical structure can be described by a single, frequency-dependent effective stiffness $K_{1,\text{eff}}(\omega)$. Following Ref. [24]:

$$K_{1,\text{eff}}(\omega) = K_1 + \frac{\lambda^2 k_3}{2} \frac{\omega^2}{\omega^2 - \omega_r^2}. \quad (6)$$

Equation (6) captures the essential physics: below resonance ($\omega < \omega_r$), the second term is negative, reducing the effective stiffness; above resonance ($\omega > \omega_r$), it is positive, increasing the stiffness. At $\omega = \omega_r$, the effective stiffness diverges ($K_{1,\text{eff}} \rightarrow \pm\infty$), and at a specific frequency ω_s (derived in the next section), it vanishes ($K_{1,\text{eff}} = 0$).

By substituting Eq. (6), the 3-DoF system reduces to an effective 2-DoF model:

$$M\ddot{U}_{1,j} + K_{1,\text{eff}}(\omega)(U_{1,j} - U_{2,j}) + K_2(U_{1,j} - U_{2,j-1}) = 0, \quad (7)$$

$$M\ddot{U}_{2,j} + K_{1,\text{eff}}(\omega)(U_{2,j} - U_{1,j}) + K_2(U_{2,j} - U_{1,j+1}) = 0. \quad (8)$$

Applying Bloch's theorem yields a 2×2 eigenvalue problem, $\mathbf{D}_{\text{eff}}(q, \omega)\mathbf{U}_{\text{eff}} = \omega^2\mathbf{U}_{\text{eff}}$, where $\mathbf{U}_{\text{eff}} = [U_1, U_2]^T$ and:

$$\mathbf{D}_{\text{eff}}(q, \omega) = \frac{1}{M} \begin{pmatrix} K_{1,\text{eff}} + K_2 & -(K_{1,\text{eff}} + K_2 e^{-iq}) \\ -(K_{1,\text{eff}} + K_2 e^{iq}) & K_{1,\text{eff}} + K_2 \end{pmatrix}. \quad (9)$$

This 2×2 formulation is structurally identical to the standard SSH model, with the crucial difference that $K_{1,\text{eff}}$ is frequency dependent. However, both formulations (in Eqs. (4) and (9)) represent the same system of three bands with one BrG and one LRG.

B. Band gap characterization and switching

We now analyze the band structure to understand wave propagation and detail the mechanism for switching the band gap type [Fig. 1(b)]. We first establish how to distinguish BrGs from LRGs and then demonstrate how their identities can be interchanged.

To facilitate a systematic parameter study, we introduce a dimerization parameter δ and a constant stiffness scale K , parametrizing the alternating couplings as:

$$K_1 = K(1 - \delta), \quad K_2 = K(1 + \delta), \quad (10)$$

with $K > 0$ and $\delta \in (-1, 1)$. This isolates δ as the primary control parameter: positive δ corresponds to weaker intracell coupling relative to intercell coupling, and vice versa. We further introduce non-dimensional quantities to express our results in universal form: stiffness ratio $\kappa_3 = k_3/(2K)$; characteristic frequency $\omega_{\text{mid}} = \sqrt{2K/M}$ (the mid-gap frequency of the unit cell without local resonators at $\delta = 0$); normalized resonator frequency $\Omega_r = \omega_r/\omega_{\text{mid}}$; and normalized frequency $\Omega = \omega/\omega_{\text{mid}}$, such that $\Omega^2 = \omega^2 M/(2K)$.

The defining characteristic that distinguishes an LRG from a BrG is the presence of an attenuation singularity—a frequency at which the spatial decay rate of evanescent waves diverges ($\text{Im}(q) \rightarrow \infty$). This singularity corresponds precisely to the vanishing of the effective stiffness, $K_{1,\text{eff}} = 0$. To find this singular frequency, we set Eq. (6) to zero and solve for ω_s^2 :

$$\omega_s^2 = \omega_r^2 \frac{K_1}{K_1 + \lambda^2 k_3/2} = \omega_r^2 \left(1 + \frac{\lambda^2 k_3}{2K_1} \right)^{-1}. \quad (11)$$

Substituting $K_1 = K(1 - \delta)$ and $k_3 = 2K\kappa_3$, and normalizing by $\omega_{\text{mid}}^2 = 2K/M$, we obtain:

$$\Omega_s = \Omega_r \left(1 + \frac{\lambda^2 \kappa_3}{1 - \delta} \right)^{-1/2}. \quad (12)$$

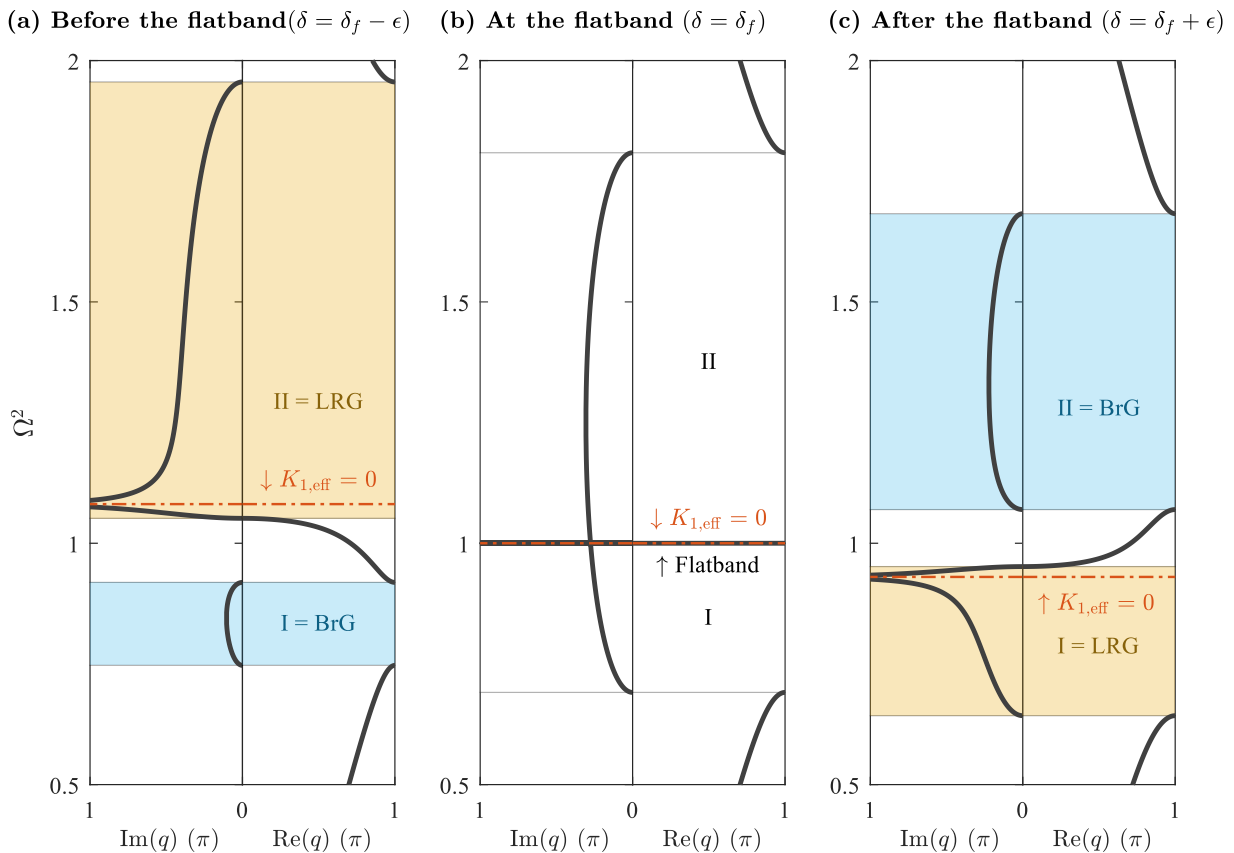


FIG. 2. **Band gap type switching via a flat band.** Orange dashed line marks $K_{1,\text{eff}} = 0$; its location defines LRG (yellow) versus BrG (blue). (a) $\delta < \delta_f$: singularity in upper gap (II = LRG). (b) $\delta = \delta_f$: singularity traversal through the flat band. (c) $\delta > \delta_f$: singularity in lower gap (I = LRG). Offset $\epsilon = 0.15\delta_f$ used in (a) and (c). Parameters: $K = 1$, $M = 1$, $k_3 = 0.5$, $m_3 = 0.2$, $\lambda = 1$.

Physically, when $K_{1,\text{eff}} = 0$, the intracell coupling vanishes, effectively decoupling adjacent unit cells and preventing wave propagation entirely. The band gap containing Ω_s is, by definition, the LRG; the gap lacking this singularity is a BrG. This interpretation aligns with previous studies tracking attenuation peaks associated with effective mass and effective stiffness [25].

Figure 2 tracks the complex band structure evolution as δ is varied. We first define a particular dimerization parameter, δ_f , where the middle branch forms a flat band [26] with zero group velocity across the entire Brillouin zone. In Fig. 2(a), where $\delta < \delta_f$, the upper gap (II) contains the singularity (orange dashed line where $\text{Im}(q) \rightarrow \infty$), identifying it as an LRG. The lower gap (I) has a bounded, arch-shaped attenuation profile characteristic of Bragg scattering, identifying it as a BrG. As δ increases, the singularity migrates from gap II to gap I. This interchange occurs at $\delta = \delta_f$, derived by finding when the middle band becomes dispersionless (see Fig. 2(b), and Supplemental Material):

$$\delta_f = \left(\frac{\kappa_3 \lambda^2 + \Omega_r^2}{2} \right) - \sqrt{\left(\frac{\kappa_3 \lambda^2 + \Omega_r^2}{2} - 1 \right)^2 + 2\lambda^2 \kappa_3}. \quad (13)$$

This flat band is a necessary intermediate state for singularity migration when sweeping the stiffness parameter δ . Within a propagating band, the wavenumber q is strictly real, whereas the attenuation singularity is a feature of the evanescent spectrum ($\text{Im}(q) \rightarrow \infty$). A dispersive band with finite bandwidth therefore acts as a spectral barrier that the singularity cannot traverse. Only when the intervening band collapses to zero bandwidth—forming a flat band—does this barrier vanish, permitting the singularity to cross from one gap to the other and thereby switch their identities [25, 27]. For $\delta > \delta_f$ [Fig. 2(c)], the singularity resides in gap I, rendering it an LRG, while gap II becomes a BrG.

C. Topological transition via band inversion

This section investigates the topological transitions arising from band gap closures—specifically, the formation of Dirac points—and the topological consequences of the gap-type switching discussed in the previous section. Our primary objective is to establish the conditions under which the LRG can host a topological phase.

To formally characterize the topology, we must first establish the relevant symmetries. The full 3×3 dynamical matrix $\mathbf{D}(q)$ is inversion symmetric [satisfying $\mathbf{P}\mathbf{D}(q)\mathbf{P}^{-1} = \mathbf{D}(-q)$], with the parity operator given as (see Supplemental Material):

$$\mathbf{P} = \begin{pmatrix} 0 & -1 & 0 \\ -1 & 0 & 0 \\ 0 & 0 & 1 \end{pmatrix}. \quad (14)$$

This 3×3 structure complicates a direct mapping to the canonical Su-Schrieffer-Heeger (SSH) model. Here, the power of the effective medium framework becomes evident: the 2×2 effective dynamical matrix $\mathbf{D}_{\text{eff}}(q)$ also preserves inversion symmetry, but in a form that allows us to utilize standard 1D topological invariants.

The inversion symmetry of the effective model is expressed as:

$$\boldsymbol{\sigma}_x \mathbf{D}_{\text{eff}}(-q) \boldsymbol{\sigma}_x^{-1} = \mathbf{D}_{\text{eff}}(q), \quad (15)$$

where the Pauli matrix $\boldsymbol{\sigma}_x$ acts as the inversion operator, swapping the two primary masses. At the high-symmetry points of the Brillouin zone ($q = 0$ and $q = \pi$), time-reversal symmetry imposes $\mathbf{D}_{\text{eff}}(-q) = \mathbf{D}_{\text{eff}}^*(q) = \mathbf{D}_{\text{eff}}(q)$ since the matrix is real. Consequently, at these points, \mathbf{D}_{eff} commutes with the inversion operator $\boldsymbol{\sigma}_x$. This commutation dictates that the eigenvectors of the Hamiltonian must essentially be simultaneous eigenvectors of $\boldsymbol{\sigma}_x$. Since the eigenvalues of $\boldsymbol{\sigma}_x$ are $+1$ and -1 , the eigenvectors at these high-symmetry points are constrained to be either symmetric (parity $+1$) or antisymmetric (parity -1):

$$\mathbf{U}_{\text{eff}}^{\text{even}} \propto \begin{pmatrix} 1 \\ 1 \end{pmatrix} \quad \text{or} \quad \mathbf{U}_{\text{eff}}^{\text{odd}} \propto \begin{pmatrix} 1 \\ -1 \end{pmatrix}. \quad (16)$$

This symmetry constraint provides a direct physical observable to probe the topology. For a symmetric eigenvector, the two masses move in phase, and the phase difference is $|\arg(U_2) - \arg(U_1)| = 0$. For an antisymmetric eigenvector, they move in anti-phase, and the phase difference is $|\arg(U_2) - \arg(U_1)| = \pi$. Therefore, monitoring this phase difference across the Brillouin zone offers a direct map of the band's parity eigenvalues. A change in this quantized phase from 0 to π (or vice versa) between $q = 0$ and $q = \pi$ signals a band inversion and a non-trivial Zak phase.

Figure 3(a) visualizes this topology by plotting the phase difference $|\arg(U_2) - \arg(U_1)|$ for all bands. We observe band gap closures at two distinct Dirac points located at $q = \pi$: The first Dirac point (DP1) occurs at $\delta = \delta_-$ (inverting the bottom and middle bands), and the second Dirac point (DP2) occurs at $\delta = \delta_+$ (inverting the middle and top bands). These critical values correspond to the condition where two bands touch each other at the Brillouin zone boundary (see Supplemental Material for derivation):

$$\delta_{\pm} = \left(\frac{\kappa_3 \lambda^2}{4} + \frac{\Omega_r^2 - 1}{2} \right) \pm \sqrt{\left(\frac{\kappa_3 \lambda^2}{4} + \frac{\Omega_r^2 - 1}{2} \right)^2 + \frac{\lambda^2 \kappa_3}{2}}. \quad (17)$$

The hierarchy of critical points is $\delta_- < \delta_f < \delta_+$. This establishes a clear sequence of transitions as δ increases: (i) a topological transition in the lower gap (I) via DP1 at δ_- ; (ii) the BrG-to-LRG character switch at δ_f ; and (iii) a topological transition in the upper gap (II) via DP2 at δ_+ . In Figure 3(b), phase change is seen, via a change in the color plotted, along $q = \pi$ at $\delta = \delta_-$ and $\delta = \delta_+$.

To formally confirm these observations, we calculate the Zak phase for each band using the discrete formulation [28]:

$$\theta_{\text{Zak}}^{(b)} = -\text{Im} \ln \left[\prod_{r=0}^{R-1} \langle \psi_b(q_r) | \psi_b(q_{r+1}) \rangle \right], \quad (|\psi_b(q_R)\rangle \equiv |\psi_b(q_0)\rangle), \quad (18)$$

where $|\psi_b\rangle$ is the normalized eigenvector. As shown in Fig. 3(c), the Zak phase jumps between 0 and π exactly at δ_{\pm} , matching the phase difference analysis. Finally, we define the gap topological invariant $\zeta^{(b)}$ as the sum of Zak phases for all bands below the gap [21, 29]:

$$\text{sgn}[\zeta^{(b)}] = (-1)^b \exp \left(i \sum_{m=1}^b \theta_{\text{Zak}}^{(m)} \right). \quad (19)$$

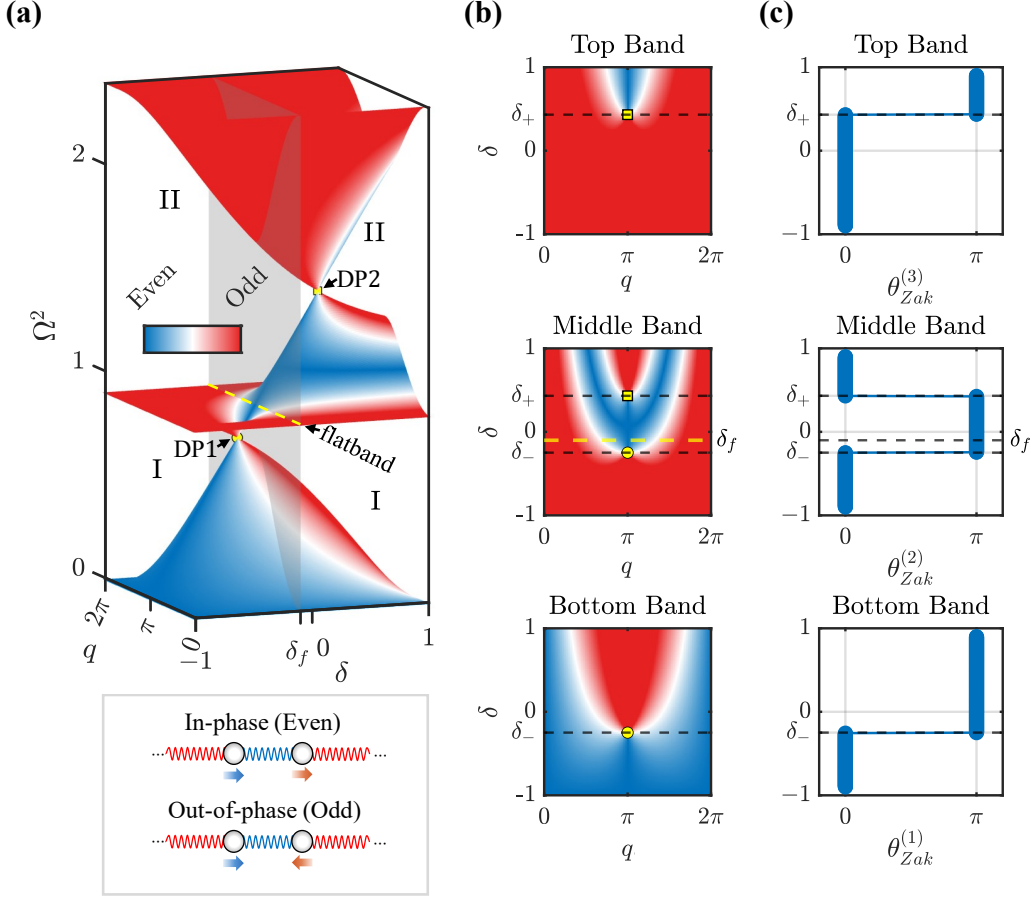


FIG. 3. **Topological phase transitions and band inversion.** (a) Band structure evolution with δ . Color map: phase difference $|\arg(U_2) - \arg(U_1)|$ (in-phase = even = blue = 0, out-of-phase = odd = red = π). DP1/DP2 mark Dirac points; dashed yellow line and the vertical gray plane indicate the flatband and δ_f , respectively. (b) Phase along the Brillouin zone versus δ for each band; phase change along $q = \pi$ shows inversion at δ_{\pm} . (c) Zak phase versus δ , confirming transitions only at δ_{\pm} . Parameters: $K = 1$, $M = 1$, $k_3 = 0.43$, $m_3 = 0.2$, $\lambda = 1$.

Table I summarizes these invariants. The most crucial finding here is the topological inheritance: the gap-type switching at δ_f does *not* alter the topological invariant. A gap that is topologically non-trivial as a BrG retains its non-trivial character even after it switches to become an LRG.

TABLE I. Sign of topological gap invariant $\zeta^{(b)}$ for intracell-resonant stiffness dimer chains.

	$\delta < \delta_-$	$\delta_- < \delta < \delta_+$	$\delta > \delta_+$
$\text{sgn}[\zeta^{(I)}]$	-	+	+
$\text{sgn}[\zeta^{(II)}]$	+	+	-

D. Finite chain spectrum and edge state localization

We now analyze the eigenfrequency spectrum of a finite chain composed of $N = 60$ unit cells with fixed boundary conditions [Fig. 4(a)]. This analysis allows for the direct observation of topological edge states that emerge within the bulk band gaps and provides a platform to verify the bulk-boundary correspondence.

As a baseline, Fig. 4(b) shows the spectrum for a standard stiffness dimer (without local resonators, *i.e.*, $K_{1,\text{eff}} = K_1$) as a function of δ . The bulk modes (black markers) form continuous bands separated by a single BrG (blue shaded region). This gap closes at $\delta = 0$ (the Dirac point) and reopens into a topologically distinct phase, giving rise to

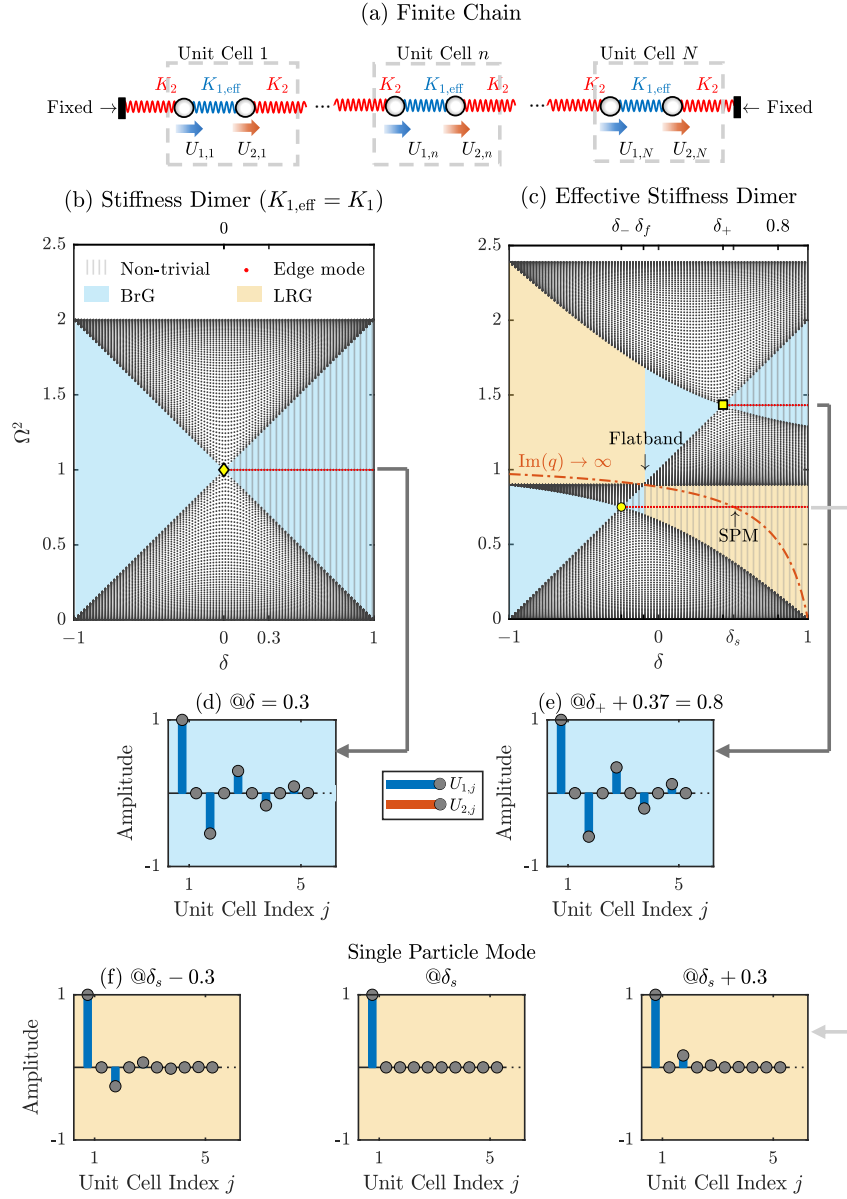


FIG. 4. **Finite-chain eigenspectra and edge states.** (a) Schematic of finite chain with fixed boundaries. (b) Standard dimer spectrum; edge modes (red markers) emerge for $\delta > 0$. (c) Effective stiffness dimer spectrum; orange curve marks $K_{1,\text{eff}} = 0$. Vertical lines: δ_- , δ_f , δ_s , δ_+ . (d) Edge mode shape in standard dimer at $\delta = 0.3$. (e) Edge mode in upper BrG at $\delta = 0.37$. (f) Edge modes in lower LRG at $\delta_s - 0.3$, δ_s , and $\delta_s + 0.3$; center shows SPM (IPR=1). Parameters: $K = 1$, $M = 1$, $k_3 = 0.43$, $m_3 = 0.2$, $\lambda = 1$, $N = 60$.

a mid-gap edge state (red markers) for $\delta > 0$. The mode shape of this edge state, shown in Fig. 4(d), exhibits the characteristic exponentially decaying profile with alternating signs between adjacent unit-cells, a hallmark of SSH-type topological modes.

For the intracell-resonant effective stiffness dimer chain, we solve the full finite eigenvalue problem. The equation of motion for the finite system is:

$$(\mathbf{D}_{3N \times 3N} - \omega^2 \mathbf{I}_{3N \times 3N}) \mathbf{u}_{3N \times 1} = \mathbf{0}_{3N \times 1}, \quad (20)$$

where the state vector is $\mathbf{u}_{3N \times 1} = [U_{1,1}, \dots, U_{1,N}, U_{2,1}, \dots, U_{2,N}, v_{3,1}, \dots, v_{3,N}]^T$. The finite dynamical matrix is

constructed as $\mathbf{D}_{3N \times 3N} = \mathbf{M}_{3N \times 3N}^{-1} \mathbf{K}_{3N \times 3N}$. The stiffness and mass matrices are given by:

$$\mathbf{K}_{3N \times 3N} = \begin{pmatrix} \mathbf{K}_{11} & \mathbf{K}_{12} & \mathbf{K}_{13} \\ \mathbf{K}_{12}^T & \mathbf{K}_{22} & \mathbf{K}_{23} \\ \mathbf{K}_{13}^T & \mathbf{K}_{23}^T & \mathbf{K}_{33} \end{pmatrix}, \quad \mathbf{M}_{3N \times 3N} = \begin{pmatrix} \mathbf{M}_{11} & \mathbf{0} & \mathbf{0} \\ \mathbf{0} & \mathbf{M}_{22} & \mathbf{0} \\ \mathbf{0} & \mathbf{0} & \mathbf{M}_{33} \end{pmatrix}, \quad (21)$$

where the sub-matrices are defined as:

$$\begin{aligned} \mathbf{K}_{11} &= \mathbf{K}_{22} = \left(K_1 + K_2 + \frac{k_3 \lambda^2}{2} \right) \mathbf{I}_{N \times N}, \\ \mathbf{K}_{12} &= \begin{pmatrix} \mathbf{0}_{1 \times (N-1)} & 0 \\ -K_2 \mathbf{I}_{(N-1) \times (N-1)} & \mathbf{0}_{(N-1) \times 1} \end{pmatrix} - \left(K_1 + \frac{k_3 \lambda^2}{2} \right) \mathbf{I}_{N \times N}, \\ \mathbf{K}_{13} &= -\mathbf{K}_{23} = -k_3 \lambda \mathbf{I}_{N \times N}, \quad \mathbf{K}_{33} = 2k_3 \mathbf{I}_{N \times N}, \\ \mathbf{M}_{11} &= \mathbf{M}_{22} = M \mathbf{I}_{N \times N}, \quad \mathbf{M}_{33} = 2m_3 \mathbf{I}_{N \times N}. \end{aligned} \quad (22)$$

Here, $\mathbf{I}_{N \times N}$ is the identity matrix and $\mathbf{0}$ represents zero matrices of appropriate dimensions.

The locally resonant (effective) stiffness dimer exhibits a richer spectrum, as shown in Fig. 4(c). We distinguish the band gap character by overlaying the frequency of the attenuation singularity (orange dashed curve), which marks the condition $K_{1,\text{eff}} = 0$. The band gap containing this singularity is the LRG (yellow region), while the gap without it is the BrG (blue region). The BrG-to-LRG switching event is clearly visible at $\delta = \delta_f$.

Consistent with the bulk topological analysis, topological edge states (red markers) emerge in each band gap once δ crosses the corresponding Dirac point. The lower gap (I) hosts an edge state for $\delta > \delta_-$, and the upper gap (II) hosts one for $\delta > \delta_+$. Figure 4(e) displays the mode shape for an edge state in the upper BrG (gap II). It shows localization similar to the standard stiffness dimer [Fig. 4(d)], with exponential decay and multi-site participation, specifically characterized by out-of-phase motion between alternating sites.

However, the unique physics of the LRG enables a novel localization phenomenon in the lower gap. When the frequency of the attenuation singularity, Ω_s , intersects the frequency of the lower topological edge state, $\Omega_{\text{edge,I}}$, a resonance condition is met. This occurs at the specific value $\delta = \delta_s$ (see Supplemental Material):

$$\delta_s = \left(\frac{\kappa_3 \lambda^2}{2} + \Omega_r^2 \right) - \sqrt{\left(\frac{\kappa_3 \lambda^2}{2} + \Omega_r^2 - 1 \right)^2 + 2\kappa_3 \lambda^2}. \quad (23)$$

At this precise point, the topological state achieves extreme localization, as illustrated in Fig. 4(f). The central panel of Fig. 4(f) ($\delta = \delta_s$) shows the mode shape confined entirely to a single primary mass at the chain's boundary, *i.e.*, a SPM. This is reminiscent of the full dimerized limit of an SSH dimer [30], but here it occurs at a finite frequency within an LRG. Notably, a transition in the edge mode profile is observed across this point: for $\delta < \delta_s$, the alternating sites oscillate out of phase, whereas for $\delta > \delta_s$, they oscillate in phase. Consequently, the SPM condition at $\delta = \delta_s$ serves as a singular crossover point between these distinct localization regimes.

We quantify this localization using the Inverse Participation Ratio (IPR):

$$\text{IPR} = \frac{\sum_{j=1}^N (U_{1,j}^4 + U_{2,j}^4)}{\left(\sum_{j=1}^N (U_{1,j}^2 + U_{2,j}^2) \right)^2}. \quad (24)$$

For the SPM at $\delta = \delta_s$, the IPR is exactly unity (considering a single boundary mode either localized on the left or the right boundary). This represents the theoretical maximum for localization in a discrete lattice. This extreme confinement arises from the synergy of two effects: the SSH-like topology ensures alternating zero amplitudes on the sub-lattice, while the vanishing effective stiffness ($K_{1,\text{eff}} \rightarrow 0$) dynamically decouples the boundary unit cell from the rest of the chain, with the local resonators precisely counterbalancing the inertial forces of the boundary mass.

E. Disorder analysis and tuned boundaries

Having established the existence of the SPM at $\delta = \delta_s$, we now address two practical questions: (i) how robust is this extreme localization to structural disorder, and (ii) can the single-particle confinement be extended from an isolated fine-tuned point to a continuous parameter range? These questions are critical for any experimental realization, where structural imperfections are unavoidable and fine-tuning a single operating point may be impractical. We address both

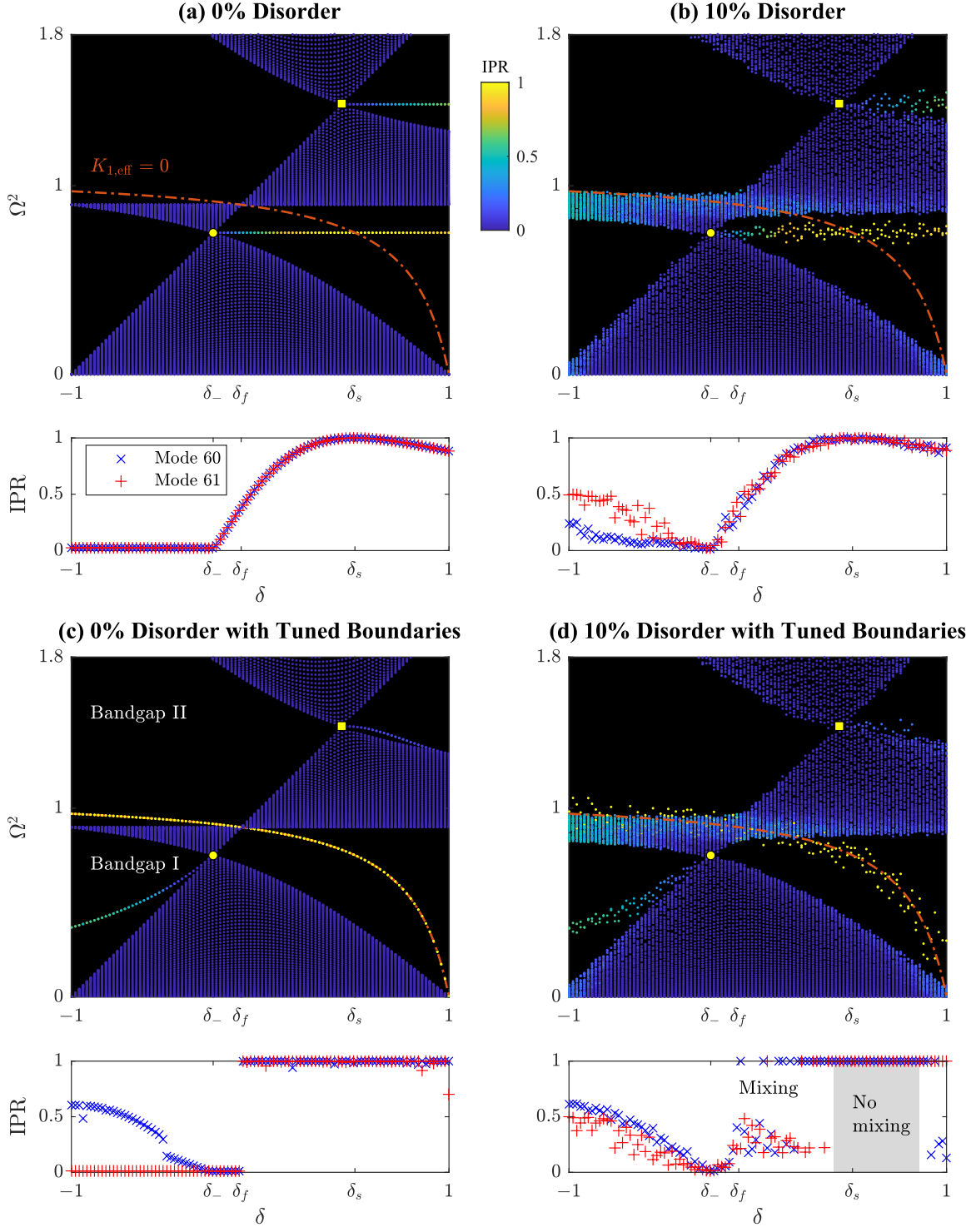


FIG. 5. **Localization and disorder with tuned boundaries.** IPR shown by color (yellow = 1, blue = minimum). Lower panels: IPR for modes 60 and 61 (LRG edge modes). (a) No disorder: IPR $\rightarrow 1$ at δ_s . (b) 10% disorder: frequencies scatter but high IPR maintained near δ_s . (c) Tuned boundaries, no disorder: edge modes track $K_{1,\text{eff}} = 0$, achieving IPR = 1 broadly. (d) Tuned boundaries, 10% disorder: robustness in “No mixing” region; hybridization in “Mixing” region.

through a combination of disorder analysis and a boundary-tuning strategy, showing that the latter not only broadens the SPM to a finite parameter window but also enhances its robustness against random perturbations.

To assess the robustness of the SPM, we introduce random disorder into the system. We assign independent random variations to every stiffness element in the finite chain (K_1 , K_2 , and k_3) according to the following scheme:

$$K_{1,j} = K(1 - \delta) + \Delta \cdot K_r^{(1,j)}, \quad (25)$$

$$K_{2,j} = K(1 + \delta) + \Delta \cdot K_r^{(2,j)}, \quad (26)$$

$$k_{3,j} = k_3 \left(1 + \frac{\Delta \cdot K_r^{(3,j)}}{K} \right), \quad (27)$$

where $K_r^{(\cdot,j)}$ are random numbers drawn from a uniform distribution over the interval $(-K, K)$, and $\Delta \in [0, 1)$ represents the disorder strength (e.g., $\Delta = 0.1$ corresponds to 10% disorder).

Figure 5 presents a comparative study of localization, quantified by the IPR, across different configurations. Figure 5(a) serves as the reference case (no disorder), showing the sharp peak in IPR reaching exactly unity at $\delta = \delta_s$ for mode numbers 60 and 61 (where the modes are arranged in an ascending order of eigen-frequencies). When 10% disorder is introduced [Fig. 5(b)], the translational symmetry is broken, and the eigenfrequencies of the edge modes scatter around the theoretical prediction. While the perfect IPR=1 condition is perturbed, the edge mode shows a degree of intrinsic robustness as it retains high localization values near δ_s .

To overcome the limitation of the SPM being created at a single design point δ_s , and to realize it across a broader range of system configurations, we propose a ‘‘tuned boundary’’ strategy. The physical intuition is to enforce the single-particle resonance condition locally at the boundaries, regardless of the bulk parameters. We achieve this by modifying the stiffness of the boundary springs ($K_{2,1}$ at the left edge and $K_{2,N+1}$ at the right edge) such that the natural frequency of the isolated boundary mass matches the frequency where the bulk effective stiffness vanishes (Ω_s). This requires satisfying the condition $K_{2,\text{boundary}}/M = \omega_s^2$, which yields the closed-form tuning expressions:

$$K_{2,1} = \frac{Mk_{3,1}}{m_3 \left(1 + \frac{\lambda^2 k_{3,1}}{2K_{1,1}} \right)}, \quad K_{2,N+1} = \frac{Mk_{3,N}}{m_3 \left(1 + \frac{\lambda^2 k_{3,N}}{2K_{1,N}} \right)}. \quad (28)$$

This tuning effectively ‘‘pins’’ the edge mode to the attenuation singularity curve ($K_{1,\text{eff}} = 0$) across the parameter space. We note that this creates a ‘‘defective’’ boundary which does not support a topological edge mode in a strict sense; however, we suggest this is of interest regarding preservation of the single particle localized edge mode. Previously, Yousef *et al.* [31] have tuned eigenfrequencies of edge modes in a BrG by tuning the edges. However, such a study in LRGs or its impact on localization remains unexplored to the best of our knowledge. The efficacy of this strategy is demonstrated in Fig. 5(c). With tuned boundaries (and no disorder), the edge mode frequency perfectly tracks the orange dashed line corresponding to the attenuation singularity. Consequently, the edge mode maintains an IPR of exactly 1 over a broad range of δ , extending the SPM from a point-like phenomenon to a stable phase across a parameter space. Note that this tuning modifies the boundary conditions sufficiently to close the gap for BrG-based edge modes, which disappear, while new edge modes appear in gap I for $\delta < \delta_-$.

Crucially, this spectral pinning enhances robustness against disorder. Figure 5(d) shows the system with tuned boundaries subject to 10% disorder. We identify two distinct regimes. In the ‘‘Mixing’’ region, where the edge mode frequency (tracking $K_{1,\text{eff}} = 0$) approaches the bulk bands, the disorder facilitates hybridization between the edge state and bulk modes, leading to delocalization. However, in the ‘‘No mixing’’ region, where the attenuation singularity is well-separated from the bulk spectrum, the tuned SPM exhibits remarkable resilience. The IPR remains close to unity, and the mode remains spectrally distinct despite significant structural randomness. This result highlights that spectral separation, combined with boundary tuning, can aid the realization of robust, ultra-localized states in practical, imperfect metamaterials.

III. CONCLUSION

In this work, we introduced a locally resonant stiffness dimer to establish a framework for generating topological edge states within LRGs. By mapping the lattice to an effective medium, we identified the attenuation singularity—where the effective stiffness vanishes—as the defining signature of the LRG. We demonstrated that this singularity can be controllably migrated between adjacent band gaps by tuning a dimerization parameter. This migration switches the gap character from BrG to LRG via an intermediate flat band state. Crucially, we showed that this switching process preserves the topological invariant (the Zak phase), allowing the system to inherit non-trivial topology from a BrG without requiring the gap closure typically associated with topological phase transitions in LRGs.

A key finding of this study is the existence of the SPM. We revealed that when a topological edge state spectrally intersects the attenuation singularity, the vibrational energy becomes confined to a single boundary particle, achieving an $\text{IPR} = 1$. This represents the theoretical maximum for localization in discrete lattices. Physically, this extreme confinement arises because the vanishing effective stiffness dynamically decouples the boundary mass from the bulk, while the local resonators precisely counterbalance inertial forces. Furthermore, this singular point marks a crossover between two distinct edge-mode regimes characterized by in-phase and out-of-phase oscillations of the sub-lattice.

Finally, we addressed the practical realizability of these states through boundary tuning. We demonstrated that by matching the boundary resonance to the bulk singularity, the SPM can be “pinned” to the zero-effective-stiffness condition over a continuous parameter range, rather than existing only at a fine-tuned point. We showed that these tuned states exhibit remarkable robustness against random disorder, provided they remain spectrally separated from the bulk bands. While demonstrated here for a 1D stiffness dimer, the underlying principles are general, suggesting that this mechanism can be extended to analogous mass-based systems [32]. These findings bridge the gap between topological mechanics and local resonance, offering a rigorous pathway to design metamaterials with ultra-localized, robust states at low frequencies.

ACKNOWLEDGMENTS

G.S.S. acknowledges financial support through the Prime Minister’s Research Fellowship (PMRF ID: 0202572). R.C. gratefully acknowledges support from the Indian Institute of Science Startup Grant. K.Q. and N.B. acknowledge support from the U.S. Army Research Office (Grant No. W911NF-20-2-0182). I.F. acknowledges support from the Department of Defense (DoD) through the National Defense Science & Engineering Graduate (NDSEG) Fellowship Program.

-
- [1] M.-H. Lu, L. Feng, and Y.-F. Chen, Phononic crystals and acoustic metamaterials, *Materials today* **12**, 34 (2009).
 - [2] J. Li and C. T. Chan, Double-negative acoustic metamaterial, *Physical Review E* **70**, 055602 (2004).
 - [3] N. Fang, D. Xi, J. Xu, M. Ambati, W. Srituravanich, C. Sun, and X. Zhang, Ultrasonic metamaterials with negative modulus, *Nature materials* **5**, 452 (2006).
 - [4] C. T. Chan, J. Li, and K. H. Fung, On extending the concept of double negativity to acoustic waves, *Journal of Zhejiang University-SCIENCE A* **7**, 24 (2006).
 - [5] Y. Ding, Z. Liu, C. Qiu, and J. Shi, Metamaterial with simultaneously negative bulk modulus and mass density, *Physical review letters* **99**, 093904 (2007).
 - [6] S. H. Lee and O. B. Wright, Origin of negative density and modulus in acoustic metamaterials, *Physical Review B* **93**, 024302 (2016).
 - [7] X. Wang, Dynamic behaviour of a metamaterial system with negative mass and modulus, *International Journal of Solids and Structures* **51**, 1534 (2014).
 - [8] L. Liu and M. I. Hussein, Wave motion in periodic flexural beams and characterization of the transition between bragg scattering and local resonance, *Journal of Applied Mechanics* **79**, 011003 (2011).
 - [9] G. Theocharis, O. Richoux, V. R. García, A. Merkel, and V. Tournat, Limits of slow sound propagation and transparency in lossy, locally resonant periodic structures, *New Journal of Physics* **16**, 093017 (2014).
 - [10] Q. Lin, J. Zhou, H. Pan, D. Xu, and G. Wen, Numerical and experimental investigations on tunable low-frequency locally resonant metamaterials, *Acta Mechanica Solida Sinica* **34**, 612 (2021).
 - [11] Y. Achaoui, A. Khelif, S. Benchabane, L. Robert, and V. Laude, Experimental observation of locally-resonant and bragg band gaps for surface guided waves in a phononic crystal of pillars, *Physical Review B—Condensed Matter and Materials Physics* **83**, 104201 (2011).
 - [12] F. Jamil, F. Chen, B. Deng, R. G. Parker, and P. Wang, Inerter-based elastic metamaterials for band gap at extremely low frequency, *Extreme Mechanics Letters* **56**, 101847 (2022).
 - [13] Y. Liu, X. Chen, and Y. Xu, Topological phononics: from fundamental models to real materials, *Advanced Functional Materials* **30**, 1904784 (2020).
 - [14] T. Shah, C. Brendel, V. Peano, and F. Marquardt, Colloquium: Topologically protected transport in engineered mechanical systems, *Rev. Mod. Phys.* **96**, 021002 (2024).
 - [15] P. Wang, L. Lu, and K. Bertoldi, Topological phononic crystals with one-way elastic edge waves, *Physical Review Letters* **115**, 104302 (2015).
 - [16] S. H. Mousavi, A. B. Khanikaev, and Z. Wang, Topologically protected elastic waves in phononic metamaterials, *Nature Communications* **6**, 8682 (2015).
 - [17] M. Serra-Garcia, V. Peri, R. Süsstrunk, O. R. Bilal, T. Larsen, L. G. Villanueva, and S. D. Huber, Observation of a phononic quadrupole topological insulator, *Nature* **555**, 342 (2018).

- [18] Q. Zhang, Y. Chen, K. Zhang, and G. Hu, Dirac degeneracy and elastic topological valley modes induced by local resonant states, *Physical Review B* **101**, 014101 (2020).
- [19] Y. Xia, A. Erturk, and M. Ruzzene, Topological edge states in quasiperiodic locally resonant metastructures, *Physical Review Applied* **13**, 014023 (2020).
- [20] C. Sugino, S. Leadham, M. Ruzzene, and A. Erturk, On the mechanism of bandgap formation in locally resonant finite elastic metamaterials, *Journal of Applied Physics* **120** (2016).
- [21] D. Zhao, M. Xiao, C. W. Ling, C. T. Chan, and K. H. Fung, Topological interface modes in local resonant acoustic systems, *Physical Review B* **98**, 014110 (2018).
- [22] Y. Jang, S. Kim, E. Kim, and J. Rho, Singular topological edge states in locally resonant metamaterials, *Science Bulletin* <https://doi.org/10.1016/j.scib.2025.01.010> (2025).
- [23] H. Zhang, L. Tang, G. Hu, Y. Li, and K. Aw, Realization of topological bragg and locally resonant interface states in one-dimensional metamaterial beam-resonator-foundation system, *Journal of Physics D: Applied Physics* **57**, 505304 (2024).
- [24] H. Huang and C. Sun, Theoretical investigation of the behavior of an acoustic metamaterial with extreme young's modulus, *Journal of the Mechanics and Physics of Solids* **59**, 2070 (2011).
- [25] A. Banerjee, S. Adhikari, and M. I. Hussein, Inertial amplification band-gap generation by coupling a levered mass with a locally resonant mass, *International Journal of Mechanical Sciences* **207**, 106630 (2021).
- [26] D. Leykam, A. Andreanov, and S. Flach, Artificial flat band systems: from lattice models to experiments, *Advances in Physics: X* **3**, 1473052 (2018).
- [27] N. M. Frandsen, O. R. Bilal, J. S. Jensen, and M. I. Hussein, Inertial amplification of continuous structures: Large band gaps from small masses, *Journal of Applied Physics* **119** (2016).
- [28] D. Vanderbilt, *Berry phases in electronic structure theory: electric polarization, orbital magnetization and topological insulators* (Cambridge University Press, 2018).
- [29] M. Xiao, Z. Zhang, and C. T. Chan, Surface impedance and bulk band geometric phases in one-dimensional systems, *Physical Review X* **4**, 021017 (2014).
- [30] J. K. Asbóth, L. Oroszlány, and A. Pályi, A short course on topological insulators, *Lecture Notes in Physics* **919** (2016).
- [31] H. Yousef, M. Nouh, *et al.*, A blueprint for truncation resonance placement in elastic diatomic lattices with unit cell asymmetry, *JASA Express Letters* **4** (2024).
- [32] F. Allein, A. Anastasiadis, R. Chaunsali, I. Frankel, N. Boechler, F. K. Diakonov, and G. Theocharis, Strain topological metamaterials and revealing hidden topology in higher-order coordinates, *Nature Communications* **14**, 6633 (2023).
- [33] Z.-Q. Jiao, S. Longhi, X.-W. Wang, J. Gao, W.-H. Zhou, Y. Wang, Y.-X. Fu, L. Wang, R.-J. Ren, L.-F. Qiao, *et al.*, Experimentally detecting quantized zak phases without chiral symmetry in photonic lattices, *Physical Review Letters* **127**, 147401 (2021).

**SUPPLEMENTARY MATERIAL:
SINGLE-PARTICLE EDGE STATE IN A LOCAL-RESONANCE-INDUCED TOPOLOGICAL BAND GAP**

I. EQUATIONS OF MOTION AND DYNAMICAL MATRICES

In this section, we derive the equations of motion and the corresponding dynamical matrices for the intracell-resonant stiffness dimer chain studied in the main text, as well as for the intercell-resonant configuration included here for completeness.

A. Intracell-resonant stiffness dimer chain

Consider an infinite quasi-one-dimensional stiffness dimer chain with local resonators attached to the intracell springs via a symmetric truss mechanism, as depicted in Fig. S1. Each unit cell contains two primary masses M (with $M_1 = M_2 = M$) constrained to horizontal motion, alternating springs K_1 (intracell) and K_2 (intercell), and a pair of identical local resonators (mass m_3 , spring k_3) coupled through hinged, massless truss members.

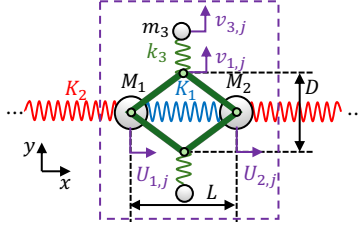


FIG. S1. Unit cell configuration of the intracell-resonant stiffness dimer chain. Primary masses M undergo horizontal displacements U_1 and U_2 , while resonator masses m_3 undergo vertical displacement v_3 . The truss geometry is characterized by parameters L and D , with $\lambda = L/D$.

The equations of motion for the j th unit cell are:

$$M\ddot{U}_{1,j} + K_1(U_{1,j} - U_{2,j}) + K_2(U_{1,j} - U_{2,j-1}) - 2k_3(v_{3,j} - v_{1,j}) \left(\frac{L}{2D} \right) = 0, \quad (\text{S1})$$

$$M\ddot{U}_{2,j} + K_1(U_{2,j} - U_{1,j}) + K_2(U_{2,j} - U_{1,j+1}) + 2k_3(v_{3,j} - v_{1,j}) \left(\frac{L}{2D} \right) = 0, \quad (\text{S2})$$

$$m_3\ddot{v}_{3,j} + k_3(v_{3,j} - v_{1,j}) = 0, \quad (\text{S3})$$

where $U_{1,j}$ and $U_{2,j}$ are the horizontal displacements of the two primary masses, $v_{3,j}$ is the vertical displacement of the resonator mass, and $v_{1,j}$ is the vertical displacement of the truss endpoint. The geometric parameters L and D characterize the massless rigid truss members, and we define $\lambda = L/D$.

The geometric constraint imposed by the rigid truss members relates the vertical displacement $v_{1,j}$ to the relative horizontal displacement $\Delta U_j = U_{2,j} - U_{1,j}$. Due to the symmetric two-bar geometry, this relative displacement is equally shared by the two inclined members, so each half-bar experiences $\Delta U_j/2$. Because the truss members maintain constant length, this relationship must satisfy:

$$\left(\frac{L}{2} + \frac{\Delta U_j}{2} \right)^2 + \left(\frac{D}{2} + v_{1,j} \right)^2 = \left(\frac{L}{2} \right)^2 + \left(\frac{D}{2} \right)^2, \quad (\text{S4})$$

which yields:

$$v_{1,j} = \frac{1}{2} \left(-D \pm \sqrt{D^2 - 2L\Delta U_j - (\Delta U_j)^2} \right). \quad (\text{S5})$$

We select the solution with the positive sign to ensure $v_{1,j} = 0$ when $\Delta U_j = 0$. For small displacements ($|\Delta U_j| \ll D, L$), we linearize by performing a Taylor expansion to first order:

$$v_{1,j} \approx -\frac{\lambda}{2}(U_{2,j} - U_{1,j}). \quad (\text{S6})$$

Substituting Eq. (S6) into Eqs. (S1)–(S3), we obtain the linearized equations of motion:

$$M\ddot{U}_{1,j} + K_1(U_{1,j} - U_{2,j}) + K_2(U_{1,j} - U_{2,j-1}) - k_3\lambda \left[v_{3,j} + \frac{\lambda}{2}(U_{2,j} - U_{1,j}) \right] = 0, \quad (\text{S7})$$

$$M\ddot{U}_{2,j} + K_1(U_{2,j} - U_{1,j}) + K_2(U_{2,j} - U_{1,j+1}) + k_3\lambda \left[v_{3,j} + \frac{\lambda}{2}(U_{2,j} - U_{1,j}) \right] = 0, \quad (\text{S8})$$

$$m_3\ddot{v}_{3,j} + k_3 \left[v_{3,j} + \frac{\lambda}{2}(U_{2,j} - U_{1,j}) \right] = 0. \quad (\text{S9})$$

These are Eqs. (1)–(3) in the main text.

Substituting Bloch wave solutions of the form $U_{1,j}(t) = U_1 e^{i(qj - \omega t)}$, $U_{2,j}(t) = U_2 e^{i(qj - \omega t)}$, and $v_{3,j}(t) = v_3 e^{i(qj - \omega t)}$ transforms the governing equations into the eigenvalue problem:

$$\mathbf{D}(q)\mathbf{U} = \omega^2\mathbf{U}, \quad (\text{S10})$$

where the eigenvector is $\mathbf{U} = [U_1, U_2, \sqrt{2m_3/M} v_3]^T$ (the scaling of v_3 ensures a Hermitian dynamical matrix), and the 3×3 dynamical matrix is:

$$\mathbf{D}(q) = \begin{pmatrix} \frac{K_1 + K_2}{M} + \frac{k_3\lambda^2}{2M} & -\left(\frac{K_1}{M} + \frac{K_2}{M}e^{-iq} + \frac{k_3\lambda^2}{2M}\right) & -\frac{k_3\lambda}{\sqrt{2Mm_3}} \\ -\left(\frac{K_1}{M} + \frac{K_2}{M}e^{iq} + \frac{k_3\lambda^2}{2M}\right) & \frac{K_1 + K_2}{M} + \frac{k_3\lambda^2}{2M} & \frac{k_3\lambda}{\sqrt{2Mm_3}} \\ -\frac{k_3\lambda}{\sqrt{2Mm_3}} & \frac{k_3\lambda}{\sqrt{2Mm_3}} & \frac{k_3}{m_3} \end{pmatrix}. \quad (\text{S11})$$

Here, $q = \tilde{\nu}d$ is the normalized wavenumber, where d is the lattice constant and $\tilde{\nu}$ is the wavenumber, and ω is the angular frequency. This is Eq. (4) in the main text.

B. Intercell-resonant stiffness dimer chain

For completeness, we also consider the intercell-resonant configuration, where the local resonators are attached to the intercell springs K_2 rather than the intracell springs K_1 , as depicted in Fig. S2.

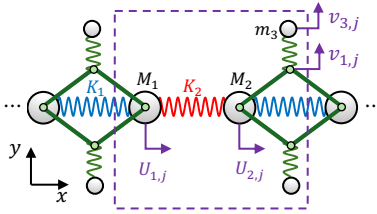


FIG. S2. Unit cell configuration of the intercell-resonant stiffness dimer chain.

The equations of motion for the j th unit cell are:

$$M\ddot{U}_{1,j} + K_1(U_{1,j} - U_{2,j-1}) + K_2(U_{1,j} - U_{2,j}) + k_3\lambda(v_{3,j-1} - v_{1,j-1}) = 0, \quad (\text{S12})$$

$$M\ddot{U}_{2,j} + K_1(U_{2,j} - U_{1,j+1}) + K_2(U_{2,j} - U_{1,j}) - k_3\lambda(v_{3,j} - v_{1,j}) = 0, \quad (\text{S13})$$

$$m_3\ddot{v}_{3,j} + k_3(v_{3,j} - v_{1,j}) = 0. \quad (\text{S14})$$

Applying the geometric constraint and linearization yields:

$$v_{1,j} \approx -\frac{\lambda}{2}(U_{1,j+1} - U_{2,j}). \quad (\text{S15})$$

Substituting this into the equations of motion gives the linearized form:

$$M\ddot{U}_{1,j} + K_1(U_{1,j} - U_{2,j-1}) + K_2(U_{1,j} - U_{2,j}) + k_3\lambda \left[v_{3,j-1} + \frac{\lambda}{2}(U_{1,j} - U_{2,j-1}) \right] = 0, \quad (\text{S16})$$

$$M\ddot{U}_{2,j} + K_1(U_{2,j} - U_{1,j+1}) + K_2(U_{2,j} - U_{1,j}) - k_3\lambda \left[v_{3,j} + \frac{\lambda}{2}(U_{1,j+1} - U_{2,j}) \right] = 0, \quad (\text{S17})$$

$$m_3\ddot{v}_{3,j} + k_3 \left[v_{3,j} + \frac{\lambda}{2}(U_{1,j+1} - U_{2,j}) \right] = 0. \quad (\text{S18})$$

Applying Bloch's theorem yields the eigenvalue problem $\mathbf{D}_{\text{intercell}}(q)\mathbf{U} = \omega^2\mathbf{U}$, where:

$$\mathbf{D}_{\text{intercell}}(q) = \begin{pmatrix} \frac{K_1 + K_2}{M} + \frac{k_3\lambda^2}{2M} & - \left(\frac{K_1}{M}e^{-iq} + \frac{K_2}{M} + \frac{k_3\lambda^2}{2M}e^{-iq} \right) & \frac{k_3e^{-iq}\lambda}{\sqrt{2Mm_3}} \\ - \left(\frac{K_1}{M}e^{iq} + \frac{K_2}{M} + \frac{k_3\lambda^2}{2M}e^{iq} \right) & \frac{K_1 + K_2}{M} + \frac{k_3\lambda^2}{2M} & - \frac{k_3\lambda}{\sqrt{2Mm_3}} \\ \frac{k_3e^{iq}\lambda}{\sqrt{2Mm_3}} & - \frac{k_3\lambda}{\sqrt{2Mm_3}} & \frac{k_3}{m_3} \end{pmatrix}. \quad (\text{S19})$$

II. INVERSION SYMMETRY ANALYSIS

In this section, we analyze the inversion symmetry of the dynamical matrices for both intracell- and intercell-resonant configurations. Inversion symmetry is a prerequisite for the quantization of the Zak phase in one-dimensional systems [33], making this analysis essential for establishing the validity of topological invariants.

We seek a parity operator \mathbf{P} that satisfies:

$$\mathbf{P}\mathbf{D}(q)\mathbf{P}^{-1} = \mathbf{D}(-q). \quad (\text{S20})$$

Since \mathbf{P} must be both Hermitian and unitary, it can be written in the general form:

$$\mathbf{P} = \begin{pmatrix} p_{11} & p_{12} & p_{13} \\ \bar{p}_{12} & p_{22} & p_{23} \\ \bar{p}_{13} & \bar{p}_{23} & p_{33} \end{pmatrix}, \quad (\text{S21})$$

where p_{11} , p_{22} , and p_{33} are real, and the overbar denotes complex conjugation. Equation (S20) can equivalently be written as:

$$\mathbf{P}\mathbf{D}(q) = \mathbf{D}(-q)\mathbf{P}. \quad (\text{S22})$$

A. Intracell-resonant configuration

We now show that the intracell-resonant stiffness dimer chain possesses inversion symmetry, and therefore the Zak phase is a valid topological invariant.

Substituting $\mathbf{D}(q) = \mathbf{D}(q)$ from Eq. (S11) into Eq. (S22) and equating matrix elements on both sides yields a system of constraints on the elements of \mathbf{P} .

Step 1: Establishing that all elements are real. Equating the (1,1) elements gives:

$$\begin{aligned} p_{11} \left(\frac{K_1 + K_2}{M} + \frac{k_3\lambda^2}{2M} \right) - p_{12} \left(\frac{K_1}{M} + \frac{K_2}{M}e^{iq} + \frac{k_3\lambda^2}{2M} \right) - p_{13} \frac{k_3\lambda}{\sqrt{2Mm_3}} \\ = p_{11} \left(\frac{K_1 + K_2}{M} + \frac{k_3\lambda^2}{2M} \right) - \bar{p}_{12} \left(\frac{K_1}{M} + \frac{K_2}{M}e^{iq} + \frac{k_3\lambda^2}{2M} \right) - \bar{p}_{13} \frac{k_3\lambda}{\sqrt{2Mm_3}}. \end{aligned} \quad (\text{S23})$$

This requires $p_{12} = \bar{p}_{12}$ and $p_{13} = \bar{p}_{13}$, implying both are real. Similarly, equating the (2,2) elements shows $p_{23} = \bar{p}_{23}$, so p_{23} is also real. Thus, all elements of \mathbf{P} are real.

Step 2: Determining diagonal elements. Equating the (1, 2) elements and rearranging:

$$(p_{11} - p_{22}) \left(\frac{K_1}{M} + \frac{k_3 \lambda^2}{2M} \right) + p_{11} \frac{K_2}{M} e^{-iq} - p_{22} \frac{K_2}{M} e^{iq} = (p_{13} + p_{23}) \frac{k_3 \lambda}{\sqrt{2Mm_3}}. \quad (\text{S24})$$

We assume the parity operator is a geometric symmetry operator independent of specific parameter values. For Eq. (S24) to hold for all q , the terms proportional to $e^{\pm iq}$ must vanish independently, yielding:

$$p_{11} = p_{22} = 0. \quad (\text{S25})$$

Substituting back into Eq. (S24) gives:

$$p_{13} + p_{23} = 0. \quad (\text{S26})$$

Step 3: Determining off-diagonal elements. Equating the (1, 3) elements with $p_{11} = p_{22} = 0$ and $p_{23} = -p_{13}$:

$$(p_{33} + p_{12}) \frac{k_3 \lambda}{\sqrt{2Mm_3}} = p_{13} \left(\frac{2K_1 + K_2(1 + e^{iq}) + k_3 \lambda^2}{M} - \frac{k_3}{m_3} \right). \quad (\text{S27})$$

For this to hold independently of parameters, both sides must vanish:

$$p_{33} + p_{12} = 0, \quad p_{13} = 0. \quad (\text{S28})$$

Combining Eqs. (S25), (S26), and (S28), the parity operator takes the form:

$$\mathbf{P} = \begin{pmatrix} 0 & -p_{33} & 0 \\ -p_{33} & 0 & 0 \\ 0 & 0 & p_{33} \end{pmatrix}. \quad (\text{S29})$$

The determinant is $|\mathbf{P}| = -p_{33}^3$. Since \mathbf{P} is real and unitary, $|\mathbf{P}| = \pm 1$, which implies $p_{33} = \pm 1$.

For $p_{33} = 1$:

$$\mathbf{P} = \mathbf{P}^\dagger = \mathbf{P}^{-1} = \begin{pmatrix} 0 & -1 & 0 \\ -1 & 0 & 0 \\ 0 & 0 & 1 \end{pmatrix}. \quad (\text{S30})$$

This is the parity operator given in the main text [Eq. (16)]. Physically, it exchanges the two primary masses ($U_1 \leftrightarrow -U_2$) while leaving the resonator coordinate unchanged, reflecting the geometric inversion center of the unit cell.

Conclusion: The dynamical matrix $\mathbf{D}(q)$ of the intracell-resonant stiffness dimer chain possesses inversion symmetry, and the Zak phase is a valid topological invariant.

B. Intercell-resonant configuration

We now show that the intercell-resonant stiffness dimer chain does *not* possess inversion symmetry in its full 3×3 representation, and therefore the Zak phase computed from the 3×3 eigenvectors is not quantized.

Substituting $\mathbf{D}(q) = \mathbf{D}_{\text{intercell}}(q)$ from Eq. (S19) into Eq. (S22) and following the same procedure as above, we first establish that all elements of \mathbf{P} are real.

Equating the (1, 2) elements and rearranging:

$$(p_{11} - p_{22}) \left(\frac{K_1}{M} e^{iq} + \frac{K_2}{M} + \frac{k_3 \lambda^2}{2M} e^{iq} \right) - p_{13} \frac{k_3 \lambda}{\sqrt{2Mm_3}} = p_{23} \frac{k_3 e^{iq} \lambda}{\sqrt{2Mm_3}}. \quad (\text{S31})$$

For this to hold for all q and all parameter values:

$$p_{11} = p_{22}, \quad p_{13} = p_{23} = 0. \quad (\text{S32})$$

Equating the (1, 3) elements with these constraints:

$$p_{11} e^{-iq} - p_{12} = p_{33} e^{iq}. \quad (\text{S33})$$

For this to hold for all q :

$$p_{11} = p_{12} = p_{33} = 0. \quad (\text{S34})$$

Combining all constraints, the parity operator becomes:

$$\mathbf{P} = \begin{pmatrix} 0 & 0 & 0 \\ 0 & 0 & 0 \\ 0 & 0 & 0 \end{pmatrix}. \quad (\text{S35})$$

Since a valid parity operator must be unitary (and hence non-singular), this null matrix cannot serve as a parity operator.

Conclusion: The dynamical matrix $\mathbf{D}_{\text{intercell}}(q)$ does not possess inversion symmetry in its 3×3 representation, and therefore the Zak phase computed from the full eigenvectors is not a valid topological invariant.

C. Effective 2×2 framework

Here we construct a reduced 2×2 effective model by eliminating the local resonator degree of freedom and analyze its inversion symmetry.

In the effective framework, $\mathbf{D}_{\text{Intracell}3 \times 3}(q)$ and $\mathbf{D}_{\text{InterCell}3 \times 3}(q)$ become

$$\mathbf{D}_{\text{intracell,eff}}(q, \omega) = \frac{1}{M} \begin{pmatrix} K_{1,\text{eff}}(\omega) + K_2 & -(K_{1,\text{eff}}(\omega) + K_2 e^{-iq}) \\ -(K_{1,\text{eff}}(\omega) + K_2 e^{iq}) & K_{1,\text{eff}}(\omega) + K_2 \end{pmatrix} \quad (\text{S36})$$

and

$$\mathbf{D}_{\text{intercell,eff}}(q, \omega) = \frac{1}{M} \begin{pmatrix} K_{1,\text{eff}}(\omega) + K_2 & -(K_{1,\text{eff}}(\omega) e^{-iq} + K_2) \\ -(K_{1,\text{eff}}(\omega) e^{iq} + K_2) & K_{1,\text{eff}}(\omega) + K_2 \end{pmatrix}, \quad (\text{S37})$$

respectively, where

$$K_{1,\text{eff}}(\omega) = K_1 + \frac{k_3 \lambda^2}{2} \frac{\omega^2}{\omega^2 - \omega_0^2} \quad (\text{S38})$$

and $\omega_0 = \sqrt{k_3/m_3}$.

We explicitly verify that the Pauli matrix σ_x ,

$$\sigma_x = \begin{pmatrix} 0 & 1 \\ 1 & 0 \end{pmatrix}, \quad (\text{S39})$$

acts as the parity operator \mathbf{P} for both reduced models, satisfying Eq. (S22), i.e.,

$$\sigma_x \mathbf{D}_{\text{intracell,eff}}(q) = \mathbf{D}_{\text{intracell,eff}}(-q) \sigma_x \quad (\text{S40})$$

and

$$\sigma_x \mathbf{D}_{\text{intercell,eff}}(q) = \mathbf{D}_{\text{intercell,eff}}(-q) \sigma_x. \quad (\text{S41})$$

Therefore, the reduced 2×2 effective intercell model is inversion symmetric, although the full 3×3 system is not. This is one of the advantages of analyzing the system in an effective framework and only keeping track of the motion of the main masses.

III. ANALYTICAL CRITERIA FOR BAND-TOUCHING AND FLAT BAND PHENOMENA

In this section, we derive analytical expressions for the band-edge frequencies at high-symmetry points in the Brillouin zone and establish the conditions for band touching (Dirac points) and flat-band formation. Throughout this section, we consider the intracell-resonant stiffness dimer chain with $M_1 = M_2 = M$, $K_1 = K(1 - \delta)$, and $K_2 = K(1 + \delta)$, where $M > 0$, $K > 0$, $\lambda > 0$, $m_3 > 0$, $k_3 > 0$, and $\delta \in (-1, 1)$.

With this parametrization, the dynamical matrix for the intercell configuration becomes:

$$\mathbf{D}(q) = \begin{pmatrix} \frac{2K}{M} + \frac{k_3\lambda^2}{2M} & -\left(\frac{K}{M}[1 - \delta + (1 + \delta)e^{-iq}] + \frac{k_3\lambda^2}{2M}\right) & -\frac{k_3\lambda}{\sqrt{2Mm_3}} \\ -\left(\frac{K}{M}[1 - \delta + (1 + \delta)e^{iq}] + \frac{k_3\lambda^2}{2M}\right) & \frac{2K}{M} + \frac{k_3\lambda^2}{2M} & \frac{k_3\lambda}{\sqrt{2Mm_3}} \\ -\frac{k_3\lambda}{\sqrt{2Mm_3}} & \frac{k_3\lambda}{\sqrt{2Mm_3}} & \frac{k_3}{m_3} \end{pmatrix}. \quad (\text{S42})$$

A. Band-edge frequencies at $q = 0$ (Brillouin zone center)

At the Brillouin zone center ($q = 0$), we have $e^{\pm iq} = 1$, and the dynamical matrix simplifies to:

$$\mathbf{D}(0) = \begin{pmatrix} \frac{2K}{M} + \frac{k_3\lambda^2}{2M} & -\left(\frac{2K}{M} + \frac{k_3\lambda^2}{2M}\right) & -\frac{k_3\lambda}{\sqrt{2Mm_3}} \\ -\left(\frac{2K}{M} + \frac{k_3\lambda^2}{2M}\right) & \frac{2K}{M} + \frac{k_3\lambda^2}{2M} & \frac{k_3\lambda}{\sqrt{2Mm_3}} \\ -\frac{k_3\lambda}{\sqrt{2Mm_3}} & \frac{k_3\lambda}{\sqrt{2Mm_3}} & \frac{k_3}{m_3} \end{pmatrix}. \quad (\text{S43})$$

Note that this matrix is independent of δ .

The eigenvalues $\omega_{0,j}^2$ (with $j \in \{1, 2, 3\}$) give the band-edge frequencies at the Brillouin zone center. Solving the characteristic equation $\det[\mathbf{D}(0) - \omega^2\mathbf{I}] = 0$ yields:

$$\omega_{0,1}^2 = 0, \quad (\text{S44})$$

$$\omega_{0,2}^2 = \frac{1}{2} \left[\left(\frac{4K + k_3\lambda^2}{M} + \frac{k_3}{m_3} \right) - \sqrt{\left(\frac{4K + k_3\lambda^2}{M} + \frac{k_3}{m_3} \right)^2 - \frac{16Kk_3}{Mm_3}} \right], \quad (\text{S45})$$

$$\omega_{0,3}^2 = \frac{1}{2} \left[\left(\frac{4K + k_3\lambda^2}{M} + \frac{k_3}{m_3} \right) + \sqrt{\left(\frac{4K + k_3\lambda^2}{M} + \frac{k_3}{m_3} \right)^2 - \frac{16Kk_3}{Mm_3}} \right]. \quad (\text{S46})$$

To verify that these eigenvalues are real and properly ordered, we examine the discriminant:

$$\left(\frac{4K + k_3\lambda^2}{M} + \frac{k_3}{m_3} \right)^2 - \frac{16Kk_3}{Mm_3} = \left(\frac{4K + k_3\lambda^2}{M} - \frac{k_3}{m_3} \right)^2 + \frac{4k_3^2\lambda^2}{Mm_3} > 0. \quad (\text{S47})$$

Since this is strictly positive, the square root is real. Furthermore:

$$0 < \sqrt{\left(\frac{4K + k_3\lambda^2}{M} + \frac{k_3}{m_3} \right)^2 - \frac{16Kk_3}{Mm_3}} < \frac{4K + k_3\lambda^2}{M} + \frac{k_3}{m_3}, \quad (\text{S48})$$

which implies $\omega_{0,2}^2 > 0$ and $\omega_{0,3}^2 > \omega_{0,2}^2$. Therefore:

$$\omega_{0,1}^2 < \omega_{0,2}^2 < \omega_{0,3}^2. \quad (\text{S49})$$

Introducing the non-dimensional parameters $\kappa_3 = k_3/(2K)$, $\Omega_r^2 = k_3M/(2Km_3)$, and the non-dimensional frequency $\Omega = \omega\sqrt{M/(2K)}$, the band-edge frequencies become:

$$\Omega_{0,1}^2 = 0, \quad (\text{S50})$$

$$\Omega_{0,2}^2 = \left(1 + \kappa_3 \lambda^2 + \frac{\Omega_r^2}{2}\right) - \sqrt{\left(1 + \kappa_3 \lambda^2 + \frac{\Omega_r^2}{2}\right)^2 - 2\Omega_r^2}, \quad (\text{S51})$$

$$\Omega_{0,3}^2 = \left(1 + \kappa_3 \lambda^2 + \frac{\Omega_r^2}{2}\right) + \sqrt{\left(1 + \kappa_3 \lambda^2 + \frac{\Omega_r^2}{2}\right)^2 - 2\Omega_r^2}. \quad (\text{S52})$$

Importantly, these band-edge frequencies at $q = 0$ are independent of the dimerization parameter δ .

B. Band-edge frequencies at $q = \pi$ (Brillouin zone edge)

At the Brillouin zone edge ($q = \pi$), we have $e^{\pm iq} = -1$, and the dynamical matrix becomes:

$$\mathbf{D}(\pi) = \begin{pmatrix} \frac{2K}{M} + \frac{k_3 \lambda^2}{2M} & \frac{2K\delta}{M} - \frac{k_3 \lambda^2}{2M} & -\frac{k_3 \lambda}{\sqrt{2Mm_3}} \\ \frac{2K\delta}{M} - \frac{k_3 \lambda^2}{2M} & \frac{2K}{M} + \frac{k_3 \lambda^2}{2M} & \frac{k_3 \lambda}{\sqrt{2Mm_3}} \\ -\frac{k_3 \lambda}{\sqrt{2Mm_3}} & \frac{k_3 \lambda}{\sqrt{2Mm_3}} & \frac{k_3}{m_3} \end{pmatrix}. \quad (\text{S53})$$

Note that this matrix depends on δ .

The eigenvalues $\omega_{\pi,j}^2$ (with $j \in \{1, 2, 3\}$) give the band-edge frequencies at the Brillouin zone edge:

$$\omega_{\pi,1}^2 = \frac{2K(1 + \delta)}{M}, \quad (\text{S54})$$

$$\omega_{\pi,2}^2 = \frac{1}{2} \left[\left(\frac{2K(1 - \delta) + k_3 \lambda^2}{M} + \frac{k_3}{m_3} \right) - \sqrt{\left(\frac{2K(1 - \delta) + k_3 \lambda^2}{M} - \frac{k_3}{m_3} \right)^2 + \frac{4k_3^2 \lambda^2}{Mm_3}} \right], \quad (\text{S55})$$

$$\omega_{\pi,3}^2 = \frac{1}{2} \left[\left(\frac{2K(1 - \delta) + k_3 \lambda^2}{M} + \frac{k_3}{m_3} \right) + \sqrt{\left(\frac{2K(1 - \delta) + k_3 \lambda^2}{M} - \frac{k_3}{m_3} \right)^2 + \frac{4k_3^2 \lambda^2}{Mm_3}} \right]. \quad (\text{S56})$$

From the structure of these expressions, we can conclude that $\omega_{\pi,2}^2 < \omega_{\pi,3}^2$, but the ordering of $\omega_{\pi,1}^2$ relative to the others depends on δ .

In non-dimensional form:

$$\Omega_{\pi,1}^2 = 1 + \delta, \quad (\text{S57})$$

$$\Omega_{\pi,2}^2 = \frac{1 - \delta}{2} + \kappa_3 \lambda^2 + \frac{\Omega_r^2}{2} - \sqrt{\left(\frac{1 - \delta}{2} + \kappa_3 \lambda^2 - \frac{\Omega_r^2}{2} \right)^2 + 2\kappa_3 \lambda^2 \Omega_r^2}, \quad (\text{S58})$$

$$\Omega_{\pi,3}^2 = \frac{1 - \delta}{2} + \kappa_3 \lambda^2 + \frac{\Omega_r^2}{2} + \sqrt{\left(\frac{1 - \delta}{2} + \kappa_3 \lambda^2 - \frac{\Omega_r^2}{2} \right)^2 + 2\kappa_3 \lambda^2 \Omega_r^2}. \quad (\text{S59})$$

All three band-edge frequencies at $q = \pi$ depend on δ .

C. Band touching at $q = \pi$ (Dirac points)

We now derive the conditions for band touching at the Brillouin zone edge. Since the band-edge frequencies at $q = 0$ are independent of δ , band touching can only occur at $q = \pi$.

First, we examine whether $\omega_{\pi,2}^2$ and $\omega_{\pi,3}^2$ can become degenerate. The discriminant under the square root in Eqs. (S55) and (S56) is:

$$\Delta_{\pi}(\delta) = \left(\frac{2K(1-\delta) + k_3\lambda^2}{M} - \frac{k_3}{m_3} \right)^2 + \frac{4k_3^2\lambda^2}{Mm_3}. \quad (\text{S60})$$

Since Δ_{π} is a sum of a squared term and a strictly positive term, it is always positive and can never vanish. Therefore, $\omega_{\pi,2}^2$ and $\omega_{\pi,3}^2$ are never degenerate.

Consequently, band touching can occur only when the first eigenvalue $\omega_{\pi,1}^2$ equals one of the other two. This condition is satisfied when:

$$\frac{2K(1+\delta)}{M} = \frac{1}{2} \left[\left(\frac{2K(1-\delta) + k_3\lambda^2}{M} + \frac{k_3}{m_3} \right) \pm \sqrt{\Delta_{\pi}(\delta)} \right]. \quad (\text{S61})$$

Solving this equation yields the critical values of δ at which band touching occurs:

$$\delta_{\pm} = \frac{1}{8K} \left(k_3\lambda^2 + \frac{2k_3M}{m_3} - 4K \pm \sqrt{\left(k_3\lambda^2 + \frac{2k_3M}{m_3} - 4K \right)^2 + 16k_3\lambda^2K} \right). \quad (\text{S62})$$

In non-dimensional form:

$$\delta_{\pm} = \left(\frac{\kappa_3\lambda^2}{4} + \frac{\Omega_r^2 - 1}{2} \right) \pm \sqrt{\left(\frac{\kappa_3\lambda^2}{4} + \frac{\Omega_r^2 - 1}{2} \right)^2 + \frac{\kappa_3\lambda^2}{2}}. \quad (\text{S63})$$

This is Eq. (19) in the main text.

From Eq. (S63), we observe that:

- The term under the square root is always positive, so δ_+ and δ_- are always real.
- Since the square root is larger than the magnitude of the first term when that term is negative, we have $\delta_- < 0 < \delta_+$ for all physically relevant parameters.

The corresponding frequencies at which band touching occurs are:

$$\omega_{\pm}^2 = \frac{2K(1+\delta_{\pm})}{M}, \quad (\text{S64})$$

or in non-dimensional form:

$$\Omega_{\pm}^2 = 1 + \delta_{\pm} = \frac{1}{2} + \frac{\kappa_3\lambda^2}{4} + \frac{\Omega_r^2}{2} \pm \sqrt{\left(\frac{\kappa_3\lambda^2}{4} + \frac{\Omega_r^2 - 1}{2} \right)^2 + \frac{\kappa_3\lambda^2}{2}}. \quad (\text{S65})$$

Rearranging Eq. (S65):

$$\Omega_{\pm}^2 = \frac{1}{2} \left[\left(1 + \frac{\kappa_3\lambda^2}{2} + \Omega_r^2 \right) \pm \sqrt{\left(1 + \frac{\kappa_3\lambda^2}{2} + \Omega_r^2 \right)^2 - 4\Omega_r^2} \right]. \quad (\text{S66})$$

These are the Dirac point frequencies mentioned in the main text. DP1 occurs at (δ_-, Ω_-^2) where the bottom and middle bands touch, and DP2 occurs at (δ_+, Ω_+^2) where the middle and top bands touch.

D. Flat-band formation condition

A flat band occurs when one of the passbands becomes dispersionless, i.e., when the band-edge frequency at $q = 0$ coincides with a band-edge frequency at $q = \pi$. For the middle band (band 2) to become flat, we require:

$$\omega_{0,2}^2 = \omega_{\pi,j}^2 \quad \text{for some } j \in \{1, 2, 3\}. \quad (\text{S67})$$

We examine each case:

Case 1: $\omega_{0,2}^2 = \omega_{\pi,2}^2$. Equating Eqs. (S45) and (S55) and solving for δ yields only $\delta = -1$, which is outside the valid range.

Case 2: $\omega_{0,2}^2 = \omega_{\pi,3}^2$. Similarly, this yields only $\delta = -1$.

Case 3: $\omega_{0,2}^2 = \omega_{\pi,1}^2$. This condition gives:

$$\frac{1}{2} \left[\left(\frac{4K + k_3\lambda^2}{M} + \frac{k_3}{m_3} \right) - \sqrt{\left(\frac{4K + k_3\lambda^2}{M} + \frac{k_3}{m_3} \right)^2 - \frac{16Kk_3}{Mm_3}} \right] = \frac{2K(1 + \delta_f)}{M}. \quad (\text{S68})$$

Solving for δ_f :

$$\delta_f = \frac{1}{4K} \left[\left(k_3\lambda^2 + \frac{k_3M}{m_3} \right) - \sqrt{\left(k_3\lambda^2 + \frac{k_3M}{m_3} - 4K \right)^2 + 16k_3\lambda^2K} \right]. \quad (\text{S69})$$

In non-dimensional form:

$$\delta_f = \frac{\kappa_3\lambda^2 + \Omega_r^2}{2} - \sqrt{\left(\frac{\kappa_3\lambda^2 + \Omega_r^2}{2} - 1 \right)^2 + 2\kappa_3\lambda^2}. \quad (\text{S70})$$

This is Eq. (14) in the main text.

The flat-band frequency is $\Omega_{0,2}$ [Eq. (S51)], which equals $\Omega_{\pi,1} = \sqrt{1 + \delta_f}$ at this condition.

IV. ZAK PHASE CHARACTERIZATION

In this section, we present numerical calculations of the Zak phase for both the full 3×3 and effective 2×2 representations of the intracell- and intercell-resonant stiffness dimer chains. These results confirm the inversion symmetry analysis of Sec. II and demonstrate the utility of the effective framework for topological characterization.

A. Zak phase calculation

The Zak phase for band b is computed using the discrete Wilson loop formulation:

$$\theta_{\text{Zak}}^{(b)} = -\text{Im} \ln \left[\prod_{r=0}^{R-1} \langle \psi_b(q_r) | \psi_b(q_{r+1}) \rangle \right], \quad \text{with } |\psi_b(q_R)\rangle \equiv |\psi_b(q_0)\rangle, \quad (\text{S71})$$

where $|\psi_b(q)\rangle$ is the normalized eigenvector of the b th band, q is the dimensionless wavenumber, $q_0 = 0$, $q_R = 2\pi$, and R is the number of discretization points in the Brillouin zone. For inversion-symmetric systems, the Zak phase is quantized to either 0 or π .

B. Results for the 3×3 representation

Figure S3 shows the band-wise Zak phase calculated from the full 3×3 dynamical matrices as a function of δ .

For the intracell-resonant configuration [Fig. S3(a)], the Zak phase is quantized to 0 or π for all three bands, confirming the inversion symmetry established in Sec. II A. The Zak phase transitions occur precisely at $\delta = \delta_-$ (where bands 1 and 2 touch at DP1) and $\delta = \delta_+$ (where bands 2 and 3 touch at DP2), consistent with the band-touching analysis in Sec. III C.

For the intercell-resonant configuration [Fig. S3(b)], the Zak phase takes non-quantized values that vary continuously with δ . This confirms the absence of inversion symmetry in the 3×3 representation, as established in Sec. II B. Consequently, the Zak phase is not a valid topological invariant for this representation.

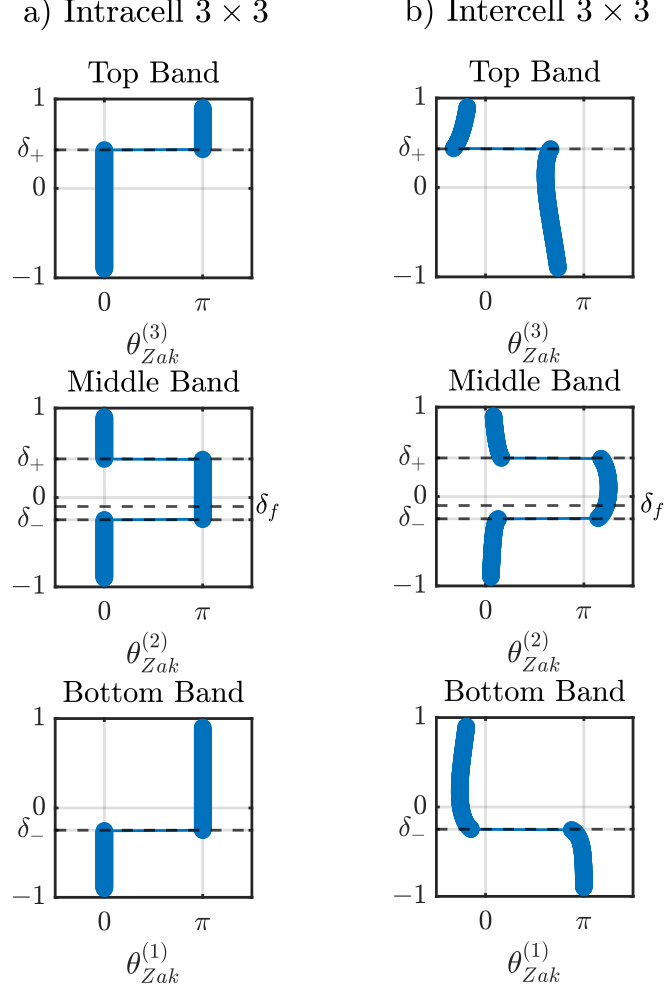


FIG. S3. Band-wise Zak phase calculated for the 3×3 dynamical matrix of (a) the intracell-resonant stiffness dimer and (b) the intercell-resonant stiffness dimer. In the intracell system (a), the Zak phase values are quantized to either 0 or π due to inversion symmetry, with transitions occurring at δ_- and δ_+ . In the intercell system (b), the Zak phase is not quantized due to the absence of inversion symmetry in the 3×3 representation. Parameters: $K = 1$, $M = 1$, $k_3 = 0.43$, $m_3 = 0.2$, $\lambda = 1$.

C. Results for the 2×2 effective representation

Figure S4 shows the band-wise Zak phase calculated from the effective 2×2 dynamical matrices.

For both configurations [Figs. S4(a) and (b)], the Zak phase is quantized to 0 or π , confirming the inversion symmetry of the effective 2×2 models established in Sec. II C. This demonstrates a key advantage of the effective framework: it enables topological characterization via the Zak phase even for systems (such as the intercell-resonant configuration) whose full 3×3 representation does not exhibit inversion symmetry.

D. Gap topological invariant

The gap topological invariant $\zeta^{(b)}$, defined in Eq. (22) of the main text, is computed from the sum of Zak phases of all bands below gap b :

$$\text{sgn}[\zeta^{(b)}] = (-1)^b \exp\left(i \sum_{m=1}^b \theta_{\text{Zak}}^{(m)}\right). \quad (\text{S72})$$

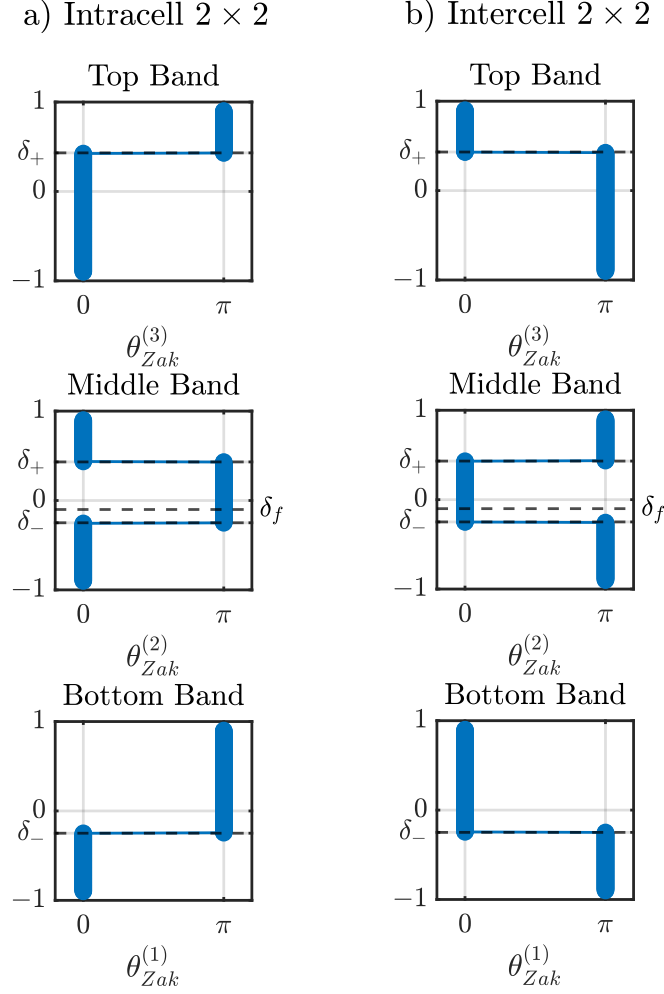


FIG. S4. Band-wise Zak phase calculated for the 2×2 effective dynamical matrix of (a) the intracell-resonant stiffness dimer and (b) the intercell-resonant stiffness dimer. In both cases, the Zak phase values are quantized to either 0 or π due to inversion symmetry in the effective framework. Parameters: $K = 1$, $M = 1$, $k_3 = 0.43$, $m_3 = 0.2$, $\lambda = 1$.

For the intracell-resonant stiffness dimer, the results are summarized in Table I of the main text. The key observation is that the gap-type switching at $\delta = \delta_f$ does not alter the topological invariant. This *topological inheritance* mechanism enables the creation of topological LRGs: a gap that becomes non-trivial as a BrG (at $\delta > \delta_-$) retains its non-trivial character after switching to an LRG (at $\delta > \delta_f$).

V. FREQUENCY OF EDGE STATES

In this section, we derive analytical expressions for the edge mode frequencies.

A. Edge mode frequencies: Standard stiffness dimer

We first derive the edge mode frequency for the standard stiffness dimer chain (without local resonators), which serves as a reference. Consider a finite chain with fixed boundaries, as shown in Fig. S5.

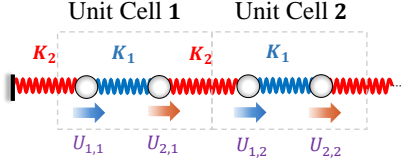
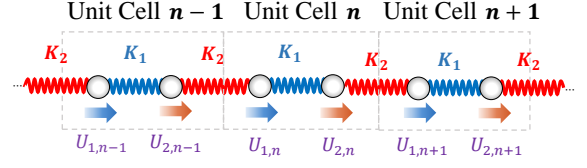
(a) At the left edge**(b) In the bulk**

FIG. S5. Finite stiffness dimer chain with fixed boundaries. (a) Left end of the chain including the first unit cell ($j = 1$). (b) A portion of the bulk centered at unit-cell index n . The displacements $U_{i,j}$ are shown, where $i \in \{1, 2\}$ indicates the sub-lattice index and j indicates the unit-cell index.

1. Equations at the edge

For the first (leftmost) unit cell, the displacements are $U_{1,1}$ and $U_{2,1}$. Assuming the edge mode decays into the bulk with a Bloch-like factor, the displacements of the second unit cell are

$$U_{1,2} = U_{1,1}e^{iq}, \quad U_{2,2} = U_{2,1}e^{iq}, \quad (\text{S73})$$

where q is complex for evanescent modes.

The equations of motion for the first unit cell (with fixed left boundary, i.e., $U_{2,0} = 0$) are

$$M\ddot{U}_{1,1} = -(K_1 + K_2)U_{1,1} + K_1U_{2,1}, \quad (\text{S74})$$

$$M\ddot{U}_{2,1} = -(K_1 + K_2)U_{2,1} + K_1U_{1,1} + K_2U_{1,2}. \quad (\text{S75})$$

Assuming harmonic motion ($\ddot{U} = -\omega^2 U$) and substituting Eq. (S73) into Eq. (S75):

$$M\omega^2 U_{1,1} = (K_1 + K_2)U_{1,1} - K_1U_{2,1}, \quad (\text{S76})$$

$$M\omega^2 U_{2,1} = (K_1 + K_2)U_{2,1} - K_1U_{1,1} - K_2U_{1,1}e^{iq}. \quad (\text{S77})$$

The characteristic equation is

$$M^2\omega^4 - 2(K_1 + K_2)M\omega^2 + K_2^2 + K_1K_2(2 - e^{iq}) = 0. \quad (\text{S78})$$

2. Equations in the bulk

For a unit cell deep in the bulk (index n), the displacements of neighboring cells are related by

$$U_{1,n\pm 1} = U_{1,n}e^{\pm iq}, \quad U_{2,n\pm 1} = U_{2,n}e^{\pm iq}. \quad (\text{S79})$$

The equations of motion are

$$M\ddot{U}_{1,n} = -(K_1 + K_2)U_{1,n} + K_1U_{2,n} + K_2U_{2,n-1}, \quad (\text{S80})$$

$$M\ddot{U}_{2,n} = -(K_1 + K_2)U_{2,n} + K_1U_{1,n} + K_2U_{1,n+1}. \quad (\text{S81})$$

The characteristic equation is

$$M^2\omega^4 - 2(K_1 + K_2)M\omega^2 + 2K_1K_2(1 - \cos(q)) = 0. \quad (\text{S82})$$

3. Frequency compatibility

For a consistent edge mode, the frequency must satisfy both the edge and bulk conditions. Equating the constant terms in Eqs. (S78) and (S82):

$$K_2^2 + K_1K_2(2 - e^{iq}) = 2K_1K_2(1 - \cos(q)). \quad (\text{S83})$$

Simplifying yields

$$e^{-iq} = -\frac{K_2}{K_1}. \quad (\text{S84})$$

Writing $q = \text{Re}(q) + i \text{Im}(q)$:

$$e^{-i \text{Re}(q)d} e^{\text{Im}(q)d} = -\frac{K_2}{K_1}. \quad (\text{S85})$$

For $K_1, K_2 > 0$, the right-hand side is negative and real, requiring

$$\text{Re}(q) = \pi, \quad e^{\text{Im}(q)} = \frac{K_2}{K_1}. \quad (\text{S86})$$

For a decaying edge mode (localized at the left boundary), we need $\text{Im}(q) > 0$, which requires

$$K_2 > K_1 \quad \Rightarrow \quad \delta > 0. \quad (\text{S87})$$

For an edge mode localized at the right boundary, the analogous analysis gives $K_1 > K_2$, i.e., $\delta < 0$. Substituting $q = \pi + i \ln(K_2/K_1)$ into the characteristic equation and solving:

$$\omega_{\text{edge,ref}}^2 = \frac{K_1 + K_2}{M}. \quad (\text{S88})$$

With $K_1 = K(1 - \delta)$ and $K_2 = K(1 + \delta)$:

$$\omega_{\text{edge,ref}}^2 = \frac{2K}{M}, \quad \text{or} \quad \Omega_{\text{edge,ref}}^2 = 1. \quad (\text{S89})$$

Key result: The edge mode frequency in the standard stiffness dimer is independent of the dimerization parameter δ .

B. Edge mode frequencies: Effective stiffness dimer

For the effective stiffness dimer, we replace K_1 with the frequency-dependent effective stiffness $K_{1,\text{eff}}(\omega)$. The edge mode frequency satisfies

$$\omega_{\text{edge}}^2 = \frac{K_{1,\text{eff}}(\omega_{\text{edge}}) + K_2}{M}. \quad (\text{S90})$$

Substituting the expression for the effective stiffness:

$$K_{1,\text{eff}}(\omega_{\text{edge}}) = K_1 + \frac{\lambda^2 k_3}{2} \frac{\omega_{\text{edge}}^2}{\omega_{\text{edge}}^2 - \omega_r^2}, \quad (\text{S91})$$

where $\omega_r = \sqrt{k_3/m_3}$.

Substituting into Eq. (S90):

$$M\omega_{\text{edge}}^2 = K_1 + K_2 + \frac{\lambda^2 k_3}{2} \frac{\omega_{\text{edge}}^2}{\omega_{\text{edge}}^2 - \omega_r^2}. \quad (\text{S92})$$

Rearranging:

$$M\omega_{\text{edge}}^2(\omega_{\text{edge}}^2 - \omega_r^2) = (K_1 + K_2)(\omega_{\text{edge}}^2 - \omega_r^2) + \frac{\lambda^2 k_3}{2} \omega_{\text{edge}}^2. \quad (\text{S93})$$

This yields a quadratic equation in ω_{edge}^2 :

$$M(\omega_{\text{edge}}^2)^2 - \left[K_1 + K_2 + M\omega_r^2 + \frac{\lambda^2 k_3}{2} \right] \omega_{\text{edge}}^2 + (K_1 + K_2)\omega_r^2 = 0. \quad (\text{S94})$$

With $K_1 + K_2 = 2K$:

$$M(\omega_{\text{edge}}^2)^2 - \left[2K + M\omega_r^2 + \frac{\lambda^2 k_3}{2}\right] \omega_{\text{edge}}^2 + 2K\omega_r^2 = 0. \quad (\text{S95})$$

Solving:

$$\omega_{\text{edge}}^2 = \frac{1}{2M} \left[\left(2K + M\omega_r^2 + \frac{\lambda^2 k_3}{2}\right) \pm \sqrt{\left(2K + M\omega_r^2 + \frac{\lambda^2 k_3}{2}\right)^2 - 8KM\omega_r^2} \right]. \quad (\text{S96})$$

This gives two edge mode frequencies:

$$\omega_{\text{edge,I}}^2 = \frac{1}{2M} \left[\left(2K + M\omega_r^2 + \frac{\lambda^2 k_3}{2}\right) - \sqrt{\left(2K + M\omega_r^2 + \frac{\lambda^2 k_3}{2}\right)^2 - 8KM\omega_r^2} \right], \quad (\text{S97})$$

$$\omega_{\text{edge,II}}^2 = \frac{1}{2M} \left[\left(2K + M\omega_r^2 + \frac{\lambda^2 k_3}{2}\right) + \sqrt{\left(2K + M\omega_r^2 + \frac{\lambda^2 k_3}{2}\right)^2 - 8KM\omega_r^2} \right]. \quad (\text{S98})$$

In nondimensional form, using $\Omega^2 = \omega^2 M / (2K)$, $\Omega_r^2 = k_3 M / (2K m_3)$, and $\kappa_3 = k_3 / (2K)$:

$$\Omega_{\text{edge,I}}^2 = \frac{1}{2} \left[\left(1 + \Omega_r^2 + \frac{\kappa_3 \lambda^2}{2}\right) - \sqrt{\left(1 + \Omega_r^2 + \frac{\kappa_3 \lambda^2}{2}\right)^2 - 4\Omega_r^2} \right], \quad (\text{S99})$$

$$\Omega_{\text{edge,II}}^2 = \frac{1}{2} \left[\left(1 + \Omega_r^2 + \frac{\kappa_3 \lambda^2}{2}\right) + \sqrt{\left(1 + \Omega_r^2 + \frac{\kappa_3 \lambda^2}{2}\right)^2 - 4\Omega_r^2} \right]. \quad (\text{S100})$$

We find that the edge mode frequencies $\Omega_{\text{edge,I}}$ in Eq. (S99) and $\Omega_{\text{edge,II}}$ in Eq. (S100), being independent of the sweeping parameter δ , are equal to Ω_- and Ω_+ in Eq. (S66), respectively.

Key result: The edge mode frequencies in the effective stiffness dimer are also independent of the dimerization parameter δ . The lower edge mode (gap I) has frequency $\Omega_{\text{edge,I}}$, and the upper edge mode (gap II) has frequency $\Omega_{\text{edge,II}}$.

VI. SINGLE-PARTICLE EDGE STATE CONDITION

In this section, we derive the condition for the single-particle mode (SPM), where the topological edge state becomes confined to a single particle at the boundary.

A. Physical mechanism

A single-particle edge state occurs when the boundary particle is effectively decoupled from the rest of the finite chain at the edge mode frequency. In the intracell-resonant configuration with fixed boundaries, this decoupling occurs when the effective intracell stiffness vanishes: $K_{1,\text{eff}}(\omega) = 0$.

At this condition, the intracell spring element (connecting the first and second particles within the unit cell) has zero effective stiffness, so the first particle oscillates independently. The natural frequency of this isolated boundary particle, connected only to the fixed wall by spring K_2 , is

$$\omega_{\text{boundary}}^2 = \frac{K_2}{M}. \quad (\text{S101})$$

For the SPM to exist, this boundary frequency must equal the frequency at which $K_{1,\text{eff}} = 0$, which is the attenuation singularity frequency ω_s :

$$\omega_s^2 = \omega_r^2 \left(1 + \frac{\lambda^2 k_3}{2K_1}\right)^{-1}. \quad (\text{S102})$$

B. Derivation of the SPM condition

The SPM condition requires

$$\omega_{\text{boundary}}^2 = \omega_s^2. \quad (\text{S103})$$

Substituting Eqs. (S101) and (S102):

$$\frac{K_2}{M} = \frac{k_3}{m_3} \left(1 + \frac{\lambda^2 k_3}{2K_1} \right)^{-1}. \quad (\text{S104})$$

Rearranging:

$$\frac{K_2}{M} \left(1 + \frac{\lambda^2 k_3}{2K_1} \right) = \frac{k_3}{m_3}. \quad (\text{S105})$$

Substituting $K_1 = K(1 - \delta)$ and $K_2 = K(1 + \delta)$:

$$\frac{K(1 + \delta)}{M} \left(1 + \frac{\lambda^2 k_3}{2K(1 - \delta)} \right) = \frac{k_3}{m_3}. \quad (\text{S106})$$

Expanding:

$$\frac{K(1 + \delta)}{M} + \frac{\lambda^2 k_3 (1 + \delta)}{2M(1 - \delta)} = \frac{k_3}{m_3}. \quad (\text{S107})$$

Multiplying through by $2M(1 - \delta)$:

$$2K(1 - \delta^2) + \lambda^2 k_3 (1 + \delta) = \frac{2M(1 - \delta)k_3}{m_3}. \quad (\text{S108})$$

Expanding and collecting terms:

$$2K - 2K\delta^2 + \lambda^2 k_3 + \lambda^2 k_3 \delta = \frac{2Mk_3}{m_3} - \frac{2Mk_3}{m_3} \delta. \quad (\text{S109})$$

Rearranging as a quadratic in δ :

$$2K\delta^2 - \left(\lambda^2 k_3 + \frac{2Mk_3}{m_3} \right) \delta - \left(2K + \lambda^2 k_3 - \frac{2Mk_3}{m_3} \right) = 0. \quad (\text{S110})$$

Using the quadratic formula:

$$\delta = \frac{\left(\lambda^2 k_3 + \frac{2Mk_3}{m_3} \right) \pm \sqrt{\left(\lambda^2 k_3 + \frac{2Mk_3}{m_3} \right)^2 + 8K \left(2K + \lambda^2 k_3 - \frac{2Mk_3}{m_3} \right)}}{4K}. \quad (\text{S111})$$

The discriminant simplifies to

$$\left(\lambda^2 k_3 + \frac{2Mk_3}{m_3} \right)^2 + 8K \left(2K + \lambda^2 k_3 - \frac{2Mk_3}{m_3} \right) = \left(\lambda^2 k_3 + \frac{2Mk_3}{m_3} - 4K \right)^2 + 16K\lambda^2 k_3. \quad (\text{S112})$$

Therefore,

$$\delta_s = \frac{1}{4K} \left[\left(\lambda^2 k_3 + \frac{2Mk_3}{m_3} \right) - \sqrt{\left(\lambda^2 k_3 + \frac{2Mk_3}{m_3} - 4K \right)^2 + 16K\lambda^2 k_3} \right], \quad (\text{S113})$$

where we have chosen the minus sign to obtain a solution in the physical range $\delta \in (-1, 1)$.

In nondimensional form, using $\kappa_3 = k_3/(2K)$ and $\Omega_r^2 = k_3 M/(2K m_3)$:

$$\delta_s = \left(\frac{\kappa_3 \lambda^2}{2} + \Omega_r^2 \right) - \sqrt{\left(\frac{\kappa_3 \lambda^2}{2} + \Omega_r^2 - 1 \right)^2 + 2\kappa_3 \lambda^2}. \quad (\text{S114})$$

C. Edge mode profile transition

The SPM condition $\delta = \delta_s$ also marks a transition in the character of the edge mode profile:

- For $\delta < \delta_s$: The edge mode decays into the bulk with alternating signs between adjacent sites (out-of-phase oscillation pattern).
- At $\delta = \delta_s$: The mode is confined to a single particle ($\text{IPR} = 1$).
- For $\delta > \delta_s$: The edge mode decays into the bulk with the same sign on adjacent sites (in-phase oscillation pattern).

This transition occurs because the effective stiffness $K_{1,\text{eff}}$ changes sign across the singularity:

- For $\omega_{\text{edge}} < \omega_s$: $K_{1,\text{eff}} > 0$ (positive effective coupling).
- At $\omega_{\text{edge}} = \omega_s$: $K_{1,\text{eff}} = 0$ (decoupled).
- For $\omega_{\text{edge}} > \omega_s$: $K_{1,\text{eff}} < 0$ (negative effective coupling).

Since the edge mode frequency $\Omega_{\text{edge,I}}$ is fixed while the singularity frequency Ω_s varies with δ , the relative position of these frequencies—and hence the sign of $K_{1,\text{eff}}$ at the edge mode frequency—changes as δ crosses δ_s .